A COMPUTATIONAL-BASED APPROACH FOR THE DESIGN OF TRIP STEELS

A Dissertation

by

SHENGYEN LI

Submitted to the Office of Graduate and Professional Studies of
Texas A&M University
in partial fulfillment of the requirements for the degree of

DOCTOR OF PHILOSOPHY

Chair of Committee,	Raymundo Arróyave
Committee Members,	Dimitris Lagoudas
	Ibrahim Karaman
	Miladin Radovic
Head of Department,	Andreas Polycarpou

August 2013

Major Subject: Mechanical Engineering

ABSTRACT

The purpose of this work is to optimize the chemical composition as well as the heat treatment for improving the mechanical performance of the TRIP steel by employing the theoretical models. TRIP steel consists of the microstructure with ferrite, bainite, retained austenite and minor martensite. Austenite contributes directly to the TRIP effect as its transformation to martensite under the external stress. In order to stabilize austenite against the martensitic transformation through the heat treatment, the two-step heat treatment is broadly applied to enrich the carbon and stabilize the austenite. During the first step of the heat treatment, intercritical annealing (IA), a dual phase structure (ferrite+austenite) is achieved. The austenite can be initially stabilized because of the low carbon solubility of ferrite. The bainite isothermal treatment (BIT) leads to the further carbon enrichment of IA-austenite by the formation of carbon-free ferrite. Comparing to the experiments, the thermodynamic and kinetic models are the lower and upper bounds of the carbon content of retained austenite. The mechanical properties are predicted using the swift model based on the predicted microstructure. In this work, a theoretical approach is coupled to a Genetic Algorithm-based optimization procedure to design (1) the heat treated temperatures to maximize the volume fraction of retained austenite in a Fe-0.32C-1.42Mn-1.56Si alloy and the chemical composition of (2) Fe-C-Mn-Si and (3) Fe-C-Mn-Si-Al-Cr-Ni alloy. The results recommend the optimum conditions of chemical composition and the heat treatment for maximizing the TRIP effect. Comparing to the experimental results, this designing strategy can be utilized to explore the potential materials of the novel alloys.

ACKNOWLEDGEMENTS

Thanks to Professor Arroyave for the mentoring; he is more than just my adviser. Thanks to Professor Karaman and Ruixian for a great collaboration. Thanks for many discussions and advise from Professor Pedro Rivera in University of Cambridge. Thanks for the financial support from US National Science Foundation, Division of Civil, Mechanical, and Manufacturing Innovation, Materials and Surface Engineering Program, Grant No. 0900187. Thanks for the help from the group-mates; you guys are the best to work with. Thanks all the support from my family in Taiwan and here, Hsiuchin. These are all the thanks behind this work, especially to you, my father.

TABLE OF CONTENTS

Page

ABSTRACT ii

ACKNOWLEDGEMENTS iii

TABLE OF CONTENTS iv

LIST OF FIGURES vi

LIST OF TABLES x

1. INTRODUCTION 1

2. LITERATURE REVIEW 4

2.1 Chemical Composition of TRIP Steel 5
2.2 Intercritical Annealing 7
2.3 Bainitic Isothermal Transformation 9
2.4 Genetic Algorithms 12

3. INTER-CRITICAL ANNEALING 14

3.1 The CALPHAD Method 14
3.2 Kinetic Model 18

4. BAINITE ISOTHERMAL TRANSFORMATION 24

4.1 Bainite Isothermal Transformation 24
4.2 Martensitic Transformation (T_{Ms}, T_{Mf}) 27
4.3 Application of the Thermodynamic Analysis to Experiments 31
4.3.1 Different T_{IA}, Constant T_{BIT} 32
4.3.2 Different T_{BIT}, Constant T_{IA} 33
4.4 Reverse Calculation 34
4.4.1 Validation 35

5. THE KINETIC MODEL FOR BAINITE ISOTHERMAL TRANSFORMATION 41

5.1 Displacive Transformation Model 42
5.2 Austenite Film 44
5.3 Calibration of Model Parameters 49

6. FINDING AN OPTIMUM HEAT TREATMENT SCHEDULE FOR TRIP-ASSISTED STEELS 56

6.1 Alloy Design 56
6.2 Predicting Mechanical Performance 57
6.3 Genetic Algorithm-based Alloy Design 61
6.4 Preliminary Evaluation of GA-based Optimization 62
6.5 Maximizing Retained Austenite of Fe-0.32C-1.42Mn-1.56Si Alloy . . . 65
6.6 The Optimum Heat Treatment Temperatures for Fe-0.32C-1.42Mn-1.56Si TRIP Steel 68

7. OPTIMIZATION OF CHEMICAL COMPOSITION IN TRIP STEEL . . 74

7.1 Fe-C-Mn-Si TRIP Steel 75
7.1.1 T_0 Limitation 75
7.1.2 Kinetics Limitation 78
7.2 Fe-C-Mn-Si-Al-Cr-Ni TRIP Steel 81

8. SUMMARY AND CONCLUSIONS 85

REFERENCES 87

APPENDIX A. CONFIGURATIONAL ENTROPY 99

LIST OF FIGURES

FIGURE Page

1.1 The schematic diagram of two-step heat treatment; (1) the dual-phase microstructure after the IA treatment (2) after quenching from T_{IA}, if T_{BIT} is lower than T_{Ms}, the martensitic transformation can be observed (3) the bainitic ferrite forms during BIT treatment (4) if the austenite is not stable enough, the martensitic transformation can not be suppressed while the alloy is cooled to room temperature 3

2.1 The stability of austenite with different C and Mn content; 1 wt% of carbon or Mn lower about 350 or 20 Kelvin difference of T_{Ms} 6

3.1 Thermodynamic analysis for Fe-0.32C-1.42Mn-1.56Si (a) phase diagram (b) the equilibrium state including the chemical composition and volume fraction of the austenite 16

3.2 The predicted T_{Ms} and Vf(Aus) after different T_{IA} treatments 17

3.3 The examination of the kinetic model for IA comparing to the work in [47] 20

3.4 The transformation of austenite at T_{IA}=1045K as function of time; the experiments are done by R. Zhu 22

3.5 The optical microscopy images (a) before ECAP (b) after ECAP 2C processing [97] 22

3.6 The predicted w_C^{γ} and volume fraction of austenite after IA under different conditions: EQ and PE are the predictions under equilibrium and para-equilibrium conditions 23

4.1 The schematic diagram for estimating the driving force for BIT[12]: ΔG_{MAX} is the maximum driving force for the nucleation of the bainite; $\Delta G^{\gamma\rightarrow\alpha}$ stands the diffusionless driving force; in order to initiate the bainitic transformation, the maximum driving force must be higher than the nucleation energy (ΔG_N); the $\Delta G^{\gamma\rightarrow\alpha}$ must be lower than -400 J/mol to keep the growing process 25

4.2 (a) The fitting curve for universal nucleation based on TCFE6 database; the empirical data is obtained from [19, 96]; (b) the effective driving force 26

4.3 The predicted martensite start temperature of Fe-0.32C-1.42Mn-1.56Si [42, 5] 28

4.4 The schematic diagram for precluding martensitic transformation at optimum T_{BIT} 29

4.5 The calculated phase diagram for BIT as T_{IA}=1045K 30

4.6 The phase diagram for BIT while (a) T_{IA}=1023K (b) T_{IA}=1083K . . 31

4.7 The volume fraction of retained austenite after two-step heat treatment (a) the same T_{BIT} and different T_{IA} (b) the same T_{IA} and different T_{BIT} [61] 33

4.8 The paired results obtained by reverse calculations; (T_{IA}=1003 K, T_{BIT}=528 K) 36

4.9 The reverse calculations while T_{IA}=1045 K comparing to the experiments 38

4.10 The schematic diagram of the heat treatment to suppress the formation of cementite 40

5.1 The schematic diagram for bainitic transformation 42

5.2 The schematic diagram for ideal BIT 46

5.3 The CCT diagram for bainitic transformation at 613 K, (a) the volume fraction of bainitic ferrite (b) the average carbon content in retained austenite as functions of time [62] 47

5.4 The decaburize time using analytical and numerical methods 48

5.5 The CCT diagram calculated by different parameters for BIT at 613 K, (a) $Vf(Bai)$ (b) w^{γ}_{C2} as functions of time 49

5.6 The comparison between different approaches to the volume of bainite sub-unit 51

5.7 The phase diagram for BIT treatment (a) the calculations by different inputs (b) comparing to the experiments [97, 62] 52

5.8 The volume fraction of retained austenite [62] 53

5.9 The diffusivity of carbon in austenite 54

6.1 The alloy designing process in this work 57

6.2 The predicted mechanical properties comparing to the experimental results [97] 59

6.3 The schematic diagram of the domain searching by genetic algorithm. 60

6.4 The schematic diagram of the genetic algorithm 63

6.5 The flow chart for optimization calculation 64

6.6 The schematic process of GA 65

6.7 The compare between different converging conditions (C.C.) (a)(c) 1% (b)(d) 5% 66

6.8 The predicted volume fraction of retained austenite while bainitic transformation stops by (a) T_0' (b) T_0 (c) kinetic model 67

6.9 The phase diagram of Fe-0.32C-1.42Mn-1.56Si after T_{IA}=1016K . . . 68

6.10 The predicted mechanical properties with fitness 70

6.11 The predicted toughness after different heat treatments based on (a) T_0' (b) T_0 (c) kinetics 71

6.12 The predicted toughness after different heat treatments 71

6.13 Phase diagrams for different heat treatments (a)-(d) for cases (1)-(4) 72

7.1 The phase diagram of Fe-0.1C (wt%) 75

7.2 The predicted fitness of the alloy with different mechanical properties 76

7.3 The relations of the mechanical properties and phase constituent . . . 77

7.4 The chemical composition of the alloy with different mechanical properties 78

7.5 The predicted mechanical properties based on kinetic limitation (a) the calculated fitness comparing to the T_0 limitation (b) the predicted toughness (MPa%) 79

7.6 The predicted mechanical properties based on T_0 limitation (a) the calculated fitness comparing to the T_0 limitation (b) the predicted toughness (MPa%) 81

7.7 The predicted mechanical properties based on T_0 limitation (a) the calculated fitness comparing to the T_0 limitation (b) the predicted toughness (MPa%) 83

7.8 The predicted mechanical properties based on T_0 limitation (a) the calculated fitness comparing to the T_0 limitation (b) the predicted toughness (MPa%) 84

8.1 The guideline for designing TRIP steel 86

LIST OF TABLES

TABLE Page

3.1 The equilibrium state of Fe-0.142C-1.35Mn-1.31Si at 1023K (the composition is in -wt%) . . . 19

3.2 The equilibrium state of Fe-0.32C-1.42Mn-1.56Si at 1016K (the composition is in -wt%) . . . 20

3.3 The equilibrium state of Fe-0.32C-1.42Mn-1.56Si at 300K (the composition is in -wt%) . . . 21

4.1 The equilibrium composition of Fe-0.32C-1.42Mn-1.56Si alloy at different T_{IA}s . . . 31

4.2 The empirical results from different heat treatments [61] . . . 32

4.3 The empirical results from different heat treatments - continued [61] . . . 32

4.4 The predicted state of the product alloy (T_{IA}=1003 K, T_{BIT}=528 K) 37

6.1 The parameters used in Swift-type equation; model A: w_C^γ=1.25 wt%; B: w_C^γ=1.5 wt%; BCC phase stands the ferrite and bainitic ferrite [56, 45] . . . 58

6.2 The heat treated temperatures (Kelvin) and time for BIT treatment in experiments; all the IAs are treated for 2 hours . . . 60

6.3 The possible variables for GA calculation (Kelvin); the string in genotype domain consists of X_1 and X_2; T_{IA} and T_{BIT} are the corresponding temperatures in phenotype domain . . . 67

6.4 The predicted mechanical properties of the four cases . . . 73

7.1 The searching domains of chemical composition and heat treated temperatures for GA calculation (-wt%) . . . 74

7.2 The optimum parameters for maximizing fitness of Fe-C-Mn-Si alloy . 80

7.3 The predicted microstructure and mechanical properties following Table 7.2 . . . 80

7.4 The optimum parameters for maximizing fitness of Fe-C-Mn-Si alloy . 82

7.5 The predicted microstructure and mechanical properties following Table 7.4; the w_C^γ, US, and UTS are in units of wt%, %, and MPa . . . 82

1. INTRODUCTION

In the automotive industry, there has been a dramatic push for the improvement of fuel economy over the past two decades. Of the many strategies available in industry, weight-reduction of the structural components of automotive systems is one of the most effective ones. While weight reduction can be accomplished through the substitution of conventional structural materials by light weight ones (sub as magnesium and aluminum alloys and carbon-based composites), a more cost-effective strategy is to dramatically increase the strength of currently used materials, such as steel alloys. Among the wide range of Advanced High Stregth Steels, TRIP-assisted steels are among the most promising alloy systems due to their low cost and extremely good mechanical proeprties (high strength and high uniform elongation).

TRIP steels typically consist of three phases: 7-15% (retained)austenite, 30-35% bainite and 50-55% ferrite [55]. The term, TRIP, stands for transformation induced plasticity. This additional plasticity is gained through the transformation, under strain, of retained austenite into martensite [11, 10]. The additional plasticity (or ductility) comes from the dissipation of mechanical energy through the phase transformation. By using the proper alloying and processing strategies, the retained austenite is stabilized (at room temperature) against athermal martensitic transformation. With careful control of the (meta)stability of the austenite phase (this is mainly accomplished through control of carbon composition), the transformation only happens during plastic deformation and this contributes to the extra plasticity exhibited by typical TRIP-assisted steels.

A typical heat treatment for TRIP steels consists of two stages: Intercritical annealing (IA) and Bainite Isothermal Treatment (BIT). During IA, the initial pearlitic

microstructure is decomposed into ferrite and austenite. The volume fractions of the two phases depends on the treatment temperature, with higher temperatures resulting in higher fractions of austenite. Since ferrite does not dissolve significant amounts of carbon, the formation of austenite is accompained by rejection of carbon from the ferrite phase [6]. With the proper selection of the IA treatment temperature, the resulting microstructure consists of the right amount of ferrite to impart sufficient baseline ductility to the TRIP steel and the right amount of austenite, with the proper carbon enrichment so it is stabilized against martensitic transformation when the alloy is taken to the lower temperature at which the bainitic transformation takes place (BIT).

During BIT, the IA ferrite remains essentially unchanged, but the retained austenite further transforms into bainite (which consists of almost carbon-free bainite as well as thin austenite films highly enriched with carbon or carbides). The transformation into bainite results in further enrichment of austenite by carbon, stabilizing it against martensitic transformation upon quenching to room temperature. The bainite phase resulting from the BIT treatment further contributes to the strength of the alloy given the very small characterstic length scale of bainitic microstructures [14]. As in IA, the temperature for the BIT treatment must be carefully selected to ensure that the austenite extists at the sufficient fraction and with the right stabity (against martensitic transformation) in order for the TRIP effect to be significant.

In this work, we investigate a base TRIP steel alloy with the nominal composition close to Fe-0.32C-1.42Mn-1.56Si. The main focus of this dissertation is to develop the appropriate thermodynamic and kinetic models to design the two-stage heat treatment (Fig. 1.1) necessary to result in optimal phase constitution that maximizes mechanical performance. In other words, the focus is to determine the proper IA (T_{IA}) and BIT temperatures to achieve optimal volume fractions of IA ferrite,

bainite, retained austenite (and martensite). In addition, the present work focuses on developing a sufficient understanding of the heat treatment so it is possible to design not only the heat treatment temperatures, but also the alloy compositions in order to maximize alloy performance.

In order to manipulate the microstructure of this complex alloy system, it is important to implement a complete theoretical model for estimating the stability of the austenite at room temperature. In this work, both thermodynamic and kinetic models are used to estimate the volume fraction of each phases during each of the stages of the IA+BIT heat treatment. This theoretical model is then coupled with Genetic Algorithm to predict the optimum chemical composition and corresponding heat treatment for optimizing the phase constitution of TRIP steels.

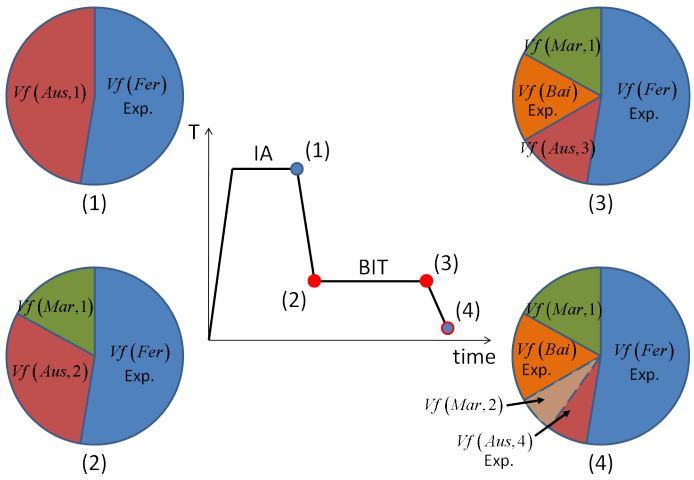

Figure 1.1: The schematic diagram of two-step heat treatment; (1) the dual-phase microstructure after the IA treatment (2) after quenching from T_{IA}, if T_{BIT} is lower than T_{Ms}, the martensitic transformation can be observed (3) the bainitic ferrite forms during BIT treatment (4) if the austenite is not stable enough, the martensitic transformation can not be suppressed while the alloy is cooled to room temperature

2. LITERATURE REVIEW

TRIP steels have outstanding mechanical properties because of the synergistic interactions of the coexisting phases that make up their microstructure [81, 68, 91]. Recent investigations indicate that after the two-step heat treatment, consisting of intercritical annealing (IA), followed by the Bainitic Isothermal Treatment (BIT) and quenching to room temperature, low alloy TRIP steels typically consist of 19.6% retained austenite and 57% ferrite, the balance being contributed by bainite as well as martensite. Typical TRIP steel alloys exhibit 31% ultimate elongation while ultimate tensile strength is 882 MPa [92]. The relatively good total elongation results from the relatively high volume fraction of retained austenite [68, 1]. While the ultimate strength of typical TRIP steels is not sufficient to constitute a realistic alternative to high strengh, light weight new-generation automotive materials, further improvement can be achieved through careful control of the alloying and processing conditions.

The key characteristic of TRIP steels is the stabilization of retained austenite against martensitic transformation. Typical TRIP steels have carbon compositions below 0.4 wt. %. This carbon content is not sufficient to prevent martensitic transformation upon quenching to room temperature, but careful control of carbon partitioning between austenite and ferrite (and bainitic ferrite) can effectively stabilize this phase. To date, there are many differnt heat treatments developed for improving the mechanical properties of TRIP steels. Quenching and Partitioning (Q & P) is one typical approach [71, 57, 22], that consists of a (partial) austenization treatment, followed by quenching and subsequent carbon partitioning of the resulting martensitic microstructure. Another common approach is the so-called two-step heat treatment [69, 81, 70, 26, 25], which consists of inter-critical annealing (IA) and

bainite isothermal transformation (BIT) treatment, followed by quenching to room temperature. The target of these processes is to enrich the remaining austenite with sufficient carbon to prevent the transformation to martensite upon cooling to room temperature. In this work, we focus on the two-stage heat treatment and we will employ fundamental thermodynamic and kinetic analysis to find the optimal alloying and processing conditions to obtain the desired phase constitution.

2.1 Chemical Composition of TRIP Steel

Conventional TRIP steel alloys have the chemical composition: Fe-(0.12-0.55)C-(0.2-0.25)Mn-(0.4-1.8)Si (wt%) [55]. The interaction between carbon, manganese and silicon is rather complicated but understanding the alloy chemistry is essential to develop optimal TRIP steels. From basic thermodyamic analyses, it is understood that C and M act as austenite stabilzers, essentially lowering the martensitc start temperature (see Fig. 2.1). While one could stabilize austenite by simply enriching the alloy with carbon, excessive carbon negatively affects the weldability of the alloys due to the formation of carbides in the weld pool as well as heat affected zones. This is the main reason why the carbon content in TRIP steels is typically limited within the 0.1 to 0.5 wt% range.

In addition of its austenite stabilizer attributes, Mn increases the solubility of carbon in austenite, further contributing to the partitioning of carbon from ferrite to austenite (particularly during IA). Unfortunately, excessive Mn may stabilze the austenite so much that it does not transform during mechanical deformation, inhibiting the TRIP effect and limiting the achievable total elongation. During the heat treatment, it is reported that the Mn may segregate at grain boundary [64]. This non-homogeneous distribution affects not only the phase transition during IA, but also the diffusion of the silicon. As mentioned, Mn preferrs to stay in austenite and

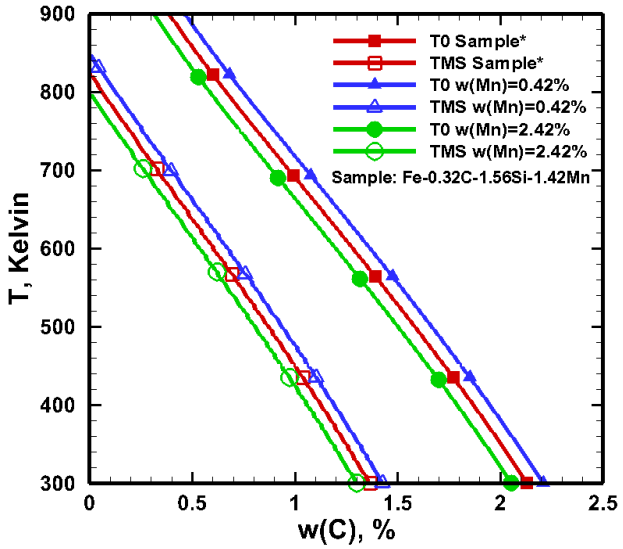

Figure 2.1: The stability of austenite with different C and Mn content; 1 wt% of carbon or Mn lower about 350 or 20 Kelvin difference of T_{Ms}

accumulates at interface on austenite side after IA [26].

Contrary to Mn, Si is more stable in ferrite. Similar to Mn, Si accumulates at austenite-ferrite interface on the ferrite side. Because Si does not dissolve in cementite, 0.8 wt% of Si can prevent the formation of cementite [55]. This is important as the formation of cementite effectively acts as a carbon sink that prevent carbon enrichment of austenite and this results in de-stabilization against martensite formation. Unfortunately, excessive Si results in problems when it comes to attempting to galvanize the alloy, which is essential for the automotive industry [66].

In TRIP steels, other elements can be used to further improve the properties of the alloys. For example, Al and P can be used to suppress the formation of cementite. Unfortunately, Al decreases the stability of austenite, relative to similar alloying contents of Si. Too much P may form Fe_3P, which results in worse performance [37]. Nb, V and Cr can be added to TRIP steels, although these elements may stabilize

ferrite and form carbides that act as carbon sinks when these consituents exceed a critical concentration [26, 55].

Since the interactions between the different constituents is rather complicated, the first stages of this research are limited to the investigation of TRIP steels that have C, Mn and Si as the major alloying elements. For the Fe-C-Mn-Si, the main goal is to determine the necessary heat treatment parameters to achieve the desired phase constitution (and by extension, the optimal mechanical performance).

2.2 Intercritical Annealing

The typical initial microstructure of low carbon steels is acombination of ferrite (α) and pearlitie (cementite + ferrite (θ)). In order to obtain high volume fraction of the austenite (γ) at room temperature, cementite must dissolve and decompose into ferrite and austenite. The minimum temperature for the intercritical annealing (IA) treatment has to be selected such that cementite is unstable against decomposition. A major target of the IA treatment is the dissolution of cementite, but after this is accomplished, the temperature must be selected to obtained the proper amount of ferrite and austenite to obtain good ductility of the final microstructure (through IA ferrite) as well as an austenite stable enough so it does not transform to martensite during subsequent heat treatments and quenching.

Dilatometric analysis is broadly applied to investigate the volume change during IA [73, 6]. The volume change is the result mainly of the formation of the ferrite+austenite microstructure. The volume expansion of ferrite takes place in the initial microstructure along with the heating process. While the temperature is higher than Ac_1, the austenite nucleates at the interface between pearlite and ferrite. Because of the low chemical potential of carbon, austenite absorbs the carbon in pearlite until the alloy reaches the temperature Ac_θ. Ac_θ is the temperature de-

fined as that at which austenite completely replaces pearlite in volume, so the carbon content in austenite is high at this temperature [83, 93, 6]. Carbon, subsequently, diffuses from austenite to ferrite which drives it transforming to austenite.

Many factors can affect the phase transformation during IA, for example, heating rate, initial microstructure and chemical composition [6, 31] etc. The interstitial elements (C and N) diffuse at very begining of the heat treatment. As the heat treatment progresses, the diffusion of the substitutional elements (Mn, Si etc.) dominates the stability of the phases. The alloying elements may seggregate to the phase interfaces, which impeds the diffusion of the other elements [59, 58]. An example is that the higher phosphorus (P) depresses silicon (Si) diffusion in ferrite and further slows the transformation rate in IA treatment. The more chemical elements in the alloy tends to slow the rate of transformation because of the partitioning between ferrite and austenite and high alloy contents usually result in very long times to achieve thermodynamic equilibrium [47, 46, 26]. For mass production, the limited heat treated time implies that the alloy never achieves equilibrium after IA treatment. As a result, thermodynamic equilibrium stands as the upper boundary of the partitioning of the substutional elements as well as the extreme case of the austenite stability.

It is reported that the alloy is heated up from room temperature to 1053K - 1153K (in general) [55]; along with the heating process, the volume of ferrite and pearlite expand because of the thermal energy. It is reported that if the alloy is cold rolled before heating, the residual stresses will be relaxed, the crystallographic texture will be changed as well [6]. More importantly, cementite will be dissoluted/spherodized and produces sufficient carbon atoms for the formation of austenite in this process [93]. While the temperature reaches Ac_θ which is defined as the cementite depleted temperature, the α to γ transformation is more obvious. Also, the carbon content

in austenite can be as high as 0.75 wt% [6].

2.3 Bainitic Isothermal Transformation

After IA, the alloy is usually quenched and held at relatively lower temperature (623K-723K, [55]) to transform the IA austenite into bainite. A proper quenching rate is required to avoid the formation of the ferrite and cementite [29]. The holding process is known as the Bainitic Isothermal Transformation (BIT) treatment. The temperature for BIT treatment (T_{BIT}) has to be lower than the bainite start temperature, T_{Bs} which can be estimated by empirical formulas [96, 19] or thermodynamic models [12, 32]. In order to suppress the formation of martensite, T_{BIT} is generally chose higher than T_{Ms}. Selecting a lower temperature results in a fraction of the IA austenite being transformed into (athermal) martensite.

While the nature of the bainitic transformation is still subject to considerable debate, in this worl we assume that the nucleation of bainitic ferrite occurs in a diffusional manner, while its growth is assume to be diffusionless. This is the so-called displacive transformation assumption for bainitic transformation. Under the displacive transformation model, the bainitic transformation is rather unique as the bainite microstructure results from a diffusional partitioning of carbon from bainite nuclei into the austenite matrix, followed by an almost instantaneous growth of bainite subunits [13, 17, 16]. Carbon diffuses out of the new forming bainite nucleus and is repelled after the growth of the bainite. Because the temperature is low, the substitutional elements do not obtain the sufficient driving forces to diffuse. From a thermodynamic view point, this condition is more consistent with the so-called para-equilibrium condition. This thermodynamic condition results when interstitials diffuse much faster than substitional elements. Under this displacive transformation model for bainitic transformation, the growth process is similar to the formation of

martensite.

The carbon content in retained austenite is also important for predicting the volume fraction of retained austenite, after BIT. While the bainitic ferrite grows at the expense of austenite, carbon is expelled from ferrite and enriches austenite. If we assume that the growth associated to the transformation is partitionless, the available driving force for the bainitic transformation steadily decreases as the remaining austenite increases its carbon content. Eventually, when the Gibbs energies of the ferrite and austenite phases are the same, the driving force completely vanishes. This thermodynamic point is known as the so-called T_0 condition. If one were to neglect any mechanical interaction between the growing bainite subunit and the austenite, the associated composition to T_0 would correspond to the maximum enrichment of austenite by carbon during BIT at a given temperature. However, in order for the bainite nucleus to grow it is necessary to overcome a so-called stored energy barrier. Accounting for this extra barrier for the bainitic transformation results in the so-called T_0' temperature, originally defined by Bhadeshia and collaborators [12]. After anlyzing multiple alloys and heat treatments, Bhadeshia and collaborators arrived at a value of 400 $Jmol^{-1}$ for this mechanical energy barrier. This extra energy barrier results in a lower limit for the maximum carbon enrichment of austenite after BIT.

As mentioned above, cementite is one of the undesired phases in TRIP steels because its formation essentially constitutes a carbon sink that prevents carbon enrichment of retained austenite. Although cementite can be dissolved by selecting the proper T_{IA}, cementite can form during the BIT treatment since the driving force for cementite formation is thermodynamically favorable. Even if the thermodynamics is favorable, this transformation is rather complex and the nucleation of cementite requires a minimum incubation time, which is in turn the result of the thermodynamic driving force as well as the relevant rates for atomic motion of carbon in the matrix.

A common strategy to control the formation of cementite during BIT is to limit the BIT time below the incubation time for a given temperature [37]. A perhaps more robust approach to control the formation of cementite during BIT is to control the treatment so the alloy never exceeds the so-called para-equilibrium austenite-cementite condition. As long as the carbon enrichment is lower than para-Eq. $\gamma - \theta$, cementite can be suppressed because of the insufficient driving force [52, 3].

While the diffusionless nature of the bainitic transformation seems to be backed up by experimental evidence [17, 16, 15], it has been observed that the carbon concentration in retained austenite is higher than the corresponding value indicated by T_0' [82, 90]. Essentially, this means that the transformation from austenite to ferrite happens even though the thermodynamic driving force is zero (or even negative). To resolve this issue, it has been suggested that the distribution of carbon in the remaining austenite is not homogeneous and a highly carbon-enriched austenite film exists adjascent to bainite subunits [54, 20]. If this hypothesis holds, this means that understanding (and controlling) the kinetics of carbon expulsion from bainitic ferrite and redistribution into retained austenite is essential to predict the maximum enrichment of austenite during BIT at arbitrary temperatures [33].

In order to understand the phase transition process during BIT, there are many semi-empirical models having been developed in order to estimate the transformation time (TTT diagram). These works can basically be divided into three categories: (1) displacive-diffusionless [34, 67, 78] (2) diffusion controlled [76, 77, 65] and (3) conventional models (Zener-Hillert type formula, Avrami equation etc. [49, 18, 38, 60, 95]. On the other hand, the diffusional controlled model is also developed for bainitic transformation. [76, 77, 65, 75]. This model is based on classic nucleation theory and Trivedi model to calculate the growth rate of the bainitic ferrite. These models are based on different physical concepts and utilizing some empirical parameters to

interpret the experimental results. They are successful at interpreting the restuls of some alloys. However, whenever the chemical composition is dramatically changed, the re-calibration of the models and the determination of new fitting parameters is required.

In this work, the emphasis is put on the carbon enrichment in retained austenite because the C is the main austenite stabilizer [81]. Thermodynamic model provides the fundamental understanding of the phase transformation include both IA and BIT. The kinetic model is employed to interpret the para-equilibrium condition during BIT and the upper bound of carbon content in retained austenite. The theoretical prediction can be utilized as the upper and lower bounds of the bainitic transformation.

2.4 Genetic Algorithms

Even if the theoretical models properly predicts the micro-structure after arbitrary heat treatment, the computational cost for sequential calculation is not affordable if one is to design a new alloy. Thus, computational algorithms are required to minimize the number of the attempts in the searching process. Genetic algorithms (GAs) a the potential method to couple the theoretical models developed to predict phase constitution as a function of heat treatment (and chemistry) to the alloy design process.

GA is a computer based optimization algorithm which imitates (to a certain degree) the process of natural evolution of populations by implementing random variation of the 'genomes' corresponding to possible solutions to the optimization problem at hand, with directed selection of the individuals that pass their genes to subsequent generations (Darwinian survival of the fittest evolution) [36, 80]. This type of optimization methodoloty is suitable for problems with non-analytical, multi-

dimensional solution landscapes and GA-based approaches have been shown to perform efficiently in a wide range of domain searching problems [85, 51]. Micro genetic algorithm (μ-GA) is one of the random-evolutionary numerical techniques in a small population. It is found that μ-GA performs very well in evolving rate which reduces the computational cost further [23]. This method has already been utilized for many alloy design investigations [89, 30, 94, 53].

In this work, we focus on the development of physics-based approaches for the prediction of phase constitution as a function of heat treatment (and alloying) in TRIP steels, while the μ-GA approach is utilized as the searching engine to locate the composition and treatment(s) that result in optimal phase constitution.

3. INTER-CRITICAL ANNEALING

As mentioned above, the inter-critical annealing (IA) treatment has the purpose of decomposing the initial ferritic+pearlitic microstructure and to form instead a dual-phase microstructure consisting of ferrite and austenite. As the cementite in pearlite is dissolved, the excess carbon is partitioned into the austenite. The temperature at which the IA treatment carried out controls the relative phase fractions between austenite and ferrite. This in turn controls the carbon enrichment of IA austenite: the more ferrite is formed, the more carbon has to be partitioned into austenite, given the very small solubility of carbon in ferrite.

The process of IA equilibration can be investigated through the use of both thermodynamic and kinetic approaches. In this chapter, the CALPHAD method is applied to estimate the equilibrium state of the alloy at each temperature, while a kinetic simulation is implemented in order to simulate the ferrite/austenite system as it approaches equilibrium. This model takes into account the finite diffusivity of the different substitutional and interstitial elements in the different phases.

3.1 The CALPHAD Method

The CALPHAD method consists of a systematic description of the phase stability of phases through the development of thermodynamic databases that contain information on how the Gibbs energies of phases depend on composition, temperature, pressure, etc. Since the process is systematic and hierarchical, CALPHAD usually enables consistent descriptions of the thermodynamic properties of phases. To date, the thermodynamics of steel alloys is perhaps one of the most successful examples of the application of the CALPHAD approach.

In a binary system, the total free energy can generally be expressed as [63]:

$$G = \sum_{1}^{2} x_k G_k^{srf} - T \cdot S^{con} + G^E \tag{3.1}$$

where x is the mole fraction of the composition.

G_k^{srf} is the free energy of the ideal mixture of the species. This is the quantity reflecting the material properties in different environments; for example, the ferromagnetic transition model is used for estimating the heat capacity changing between ferromagnetic and paramagnetic states as well as the high order polynomial as function of temperature for the regular change with temperature. There are also many other models for different proposed conditions are included in the thermodynamic database.

S^{con} is the configuration entropy which corresponds to the random mixing of the species and can be expressed as [27]:

$$S^{con} = -R[x_1 ln(x_1) + x_2 ln(x_2)] \tag{3.2}$$

G^E is the excess Gibbs free energy which is the results from non-idea mixing of the solution and can be written as [63]

$$G^E = x_1 x_2 \frac{z}{2}[E_{12} - 0.5(E_{11} + E_{22})] \tag{3.3}$$

x_1 and x_2 are the mole fraction of species 1 and 2. z is the number of bonds. E_{11}, E_{22} and E_{12} are the bonding energies between atoms 1-1, 2-2 and 1-2. The Gibbs free energy of the phase therefore can be calculated based on parameters that can be determined trough phase equilibrium experiments, thermochemical measurements as well as first-principles calculations.

In this work, the commercial code TQ interface developed by Thermocalc is utilized to access the TCFE6 (V6.2) and MOBFE1 (V1.0) databases, which are the state of the art thermodynamic and kinetic databases for steel alloys, respectively. Some subroutines from TQ interface are also embedded in the calculating processes for calculating Gibbs free energy, and chemical composition in each phases, determining the thermodynamic equilibrium state, etc.

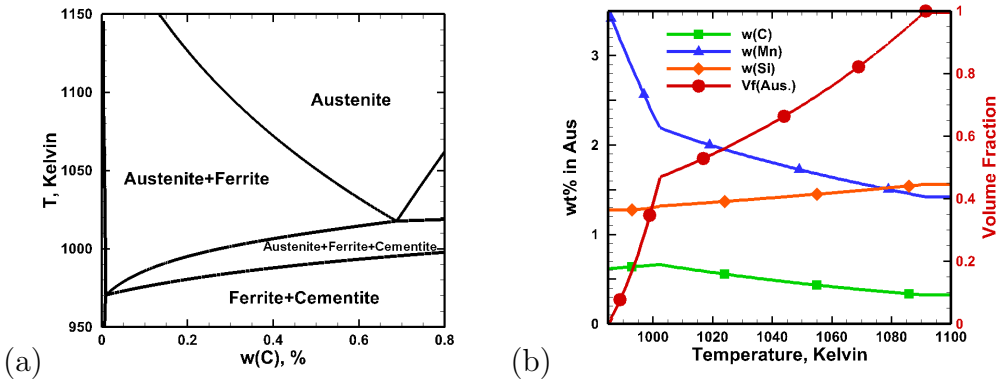

Figure 3.1: Thermodynamic analysis for Fe-0.32C-1.42Mn-1.56Si (a) phase diagram (b) the equilibrium state including the chemical composition and volume fraction of the austenite

Phase diagrams of systems can be calculated through the minimization of the total free energy of the system (as Fig 3.1). In this work, thermodynamic calculations were used to calculate the phase diagram of a typical TRIP-steel composition. As shown in Fig. 3.1(a), austenite can be observed at temperatures higher than 985 K (Ac_1). In order to stabilize austenite, higher carbon (C) and manganese (Mn) concentrations are necessary. Because cementite is dissolved completely at 1003 K (Ac_θ), austenite has a maximum C concentration, while the Mn content decreases with larger austenite phase fraction.

A simple prediction for the stability of austenite against its martensitic transformation upon quenching can be made according to the equation developed by Ishida[42]:

$$T_{Ms} = 818 - 330w_C - 23w_{Mn} - 7w_{Si} \tag{3.4}$$

where, the concentration is in weight percent (wt%). According to the composition in austenite (Fig. 3.1(b)), T_{Ms} is about 526 K when the composition of austenite corresponds to the equilibrium state at 985 K (Fig. 3.2). On the other hand, when the composition of austenite corresponds to the equilibrium state at 1003 K, T_{Ms} is about 541 K.From these simple calculations, it can be seen that the lower T_{IA} produces more stable austenite, however, its volume fraction is diminished.

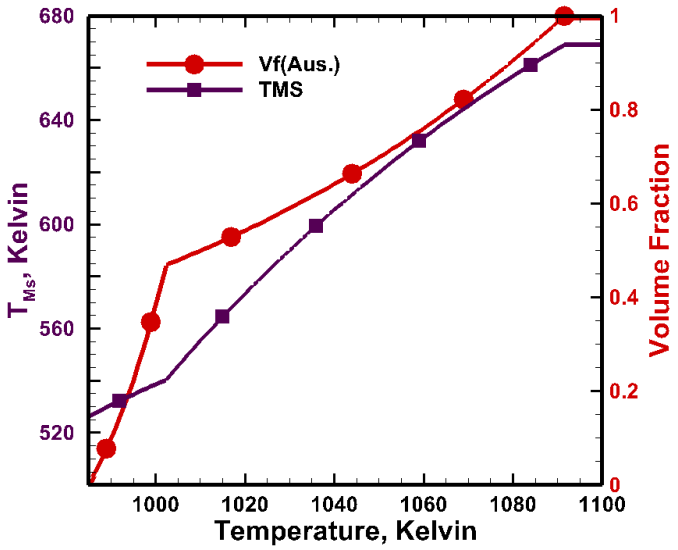

Figure 3.2: The predicted T_{Ms} and Vf(Aus) after different T_{IA} treatments

The existence of ferrite (IA-ferrite) in the microstructure of TRIP-assisted steels

is important as well, since this phase contributes—due to its softness—in great part to the ductility of the alloy. While T_{IA} is higher than Ac_θ, the transformation of the austenite consumes ferrite which dilutes the carbon concentration in austenite. Therefore, it can be proposed that under full equilibrium assumption, IA treatment is preferred at Ac_θ. However, it is clear that under equilibrium condition, the existence of cementite causes very different the composition in austenite especially with regards to Mn and C. It also affects the following quenching and BIT treatment and they will be discussed in the coming chapter.

3.2 Kinetic Model

As the base alloy is heated from room temperature to T_{IA}, austenite nucleates at the ferrite grain boundary. Because cementite provides sufficient carbon, the growing austenite firstly consumes the cementite phase until it is depleted (at temperature Ac_θ) [6]. Following the diffusion of the chemical constituents of the alloy, ferrite transforms into austenite until the alloy reaches full equilibrium. The particular phase fractions of the constituents of the dual-phase IA microstructure depends on the temperature of the treatment, T_{IA}.

To simulate the reaction of the alloy during IA, the diffusion controlled, one-dimentional model, implemented in DICTRA is used [59, 58, 47, 46, 7]. According to Fick's first and second law, the species k diffusing in phase i can be described as:

$$J_k^i = -D_k^i \frac{\partial w_k^i}{\partial x} \tag{3.5}$$

$$\frac{\partial w_k^i}{\partial t} = \frac{\partial}{\partial x}(D_k^i \frac{\partial w_k^i}{\partial x}) \tag{3.6}$$

The diffusion coefficient D_k^i can be calculated by the driving force $(\partial \mu_k^i / \partial c_k^i)$ and phenomenological parameter which is obtained from thermodynamic database,

TCFE6 (V6.2), and kinetic database, Mobfe1 (V1.0) [4, 7].

Due to the concentration difference, by mass conservation, the interface velocity, $v_{int}^{\gamma-\alpha}$ can be presented as:

$$v_{int.}^{\gamma-\alpha} = \frac{J_k^{\gamma} - J_k^{\alpha}}{w_k^{\gamma} - w_k^{\alpha}} \tag{3.7}$$

w_k^{γ} and w_k^{α} are the concentration of the k species at $\gamma - \alpha$ interface on γ and α sides.

In this work, a commercial software – DICTRA (V26), is utilized to simulate the phase transformation. Because the dissolution rate of cementite is much faster than the ferrite-austenite transformation, the initial conditions for the simulation are assumed as equilibrium at the temperature higher than Ac_{θ}. Fe-0.142C-1.35Mn-1.31Si is the alloy examined by Katsamas et al. [47, 46]. The alloy is assumed to be at the equilibrium state at 1023 K (750^oC) at which the volume fraction of ferrite and austenite and the chemical composition in each phase are listed in Table 3.1. Based on this initial condition, the alloy is simulated as being heated up to 1053 K, 1083 K, 1123 K, 1143 K and 1223 K at a rate of 10^oC/s. Whenever the system reaches the desired temperature, the alloy is held at this temperature for 90 seconds. Fig. 3.3 shows the present calculations. Our calculations show good agreement with the work done by Katsamas et al. [47, 46].

Table 3.1: The equilibrium state of Fe-0.142C-1.35Mn-1.31Si at 1023K (the composition is in -wt%)

	Vf	w_C	w_{Mn}	w_{Si}
Austenite	0.285	0.47	2.42	1.08
Ferrite	0.715	1.15E-2	0.92	1.40

With an alloy with the nominal composition of Fe-0.32C-1.42Mn-1.56Si, the full equilibrium Ac_{θ} is about 1003 K, therefore, the initial conditions should be higher

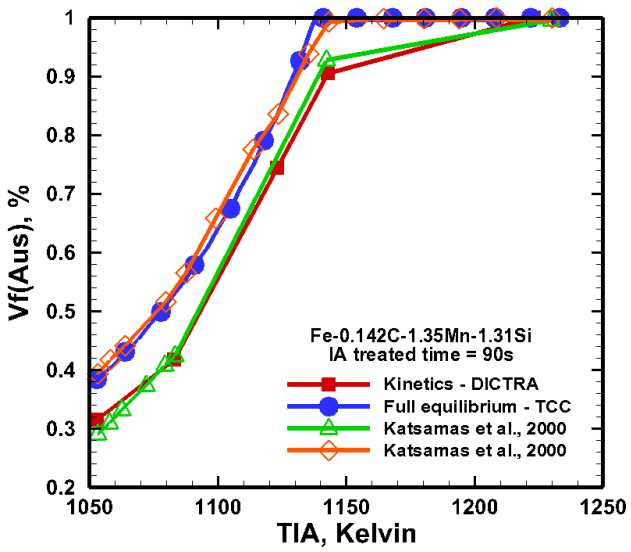

Figure 3.3: The examination of the kinetic model for IA comparing to the work in [47]

than this temperature and it is chosen as 1016 K in this work (as Table 3.2). The grain size is determined from experimental characterization to be about $10\mu m$. The alloy is heated from 1016 K by 10 K/s to 1045 K and subsequently held until equilibrium is reached. After the testing of the grid size, 128 grid points are used.

Table 3.2: The equilibrium state of Fe-0.32C-1.42Mn-1.56Si at 1016K (the composition is in -wt%)

	Vf	w_C	w_{Mn}	w_{Si}
Austenite	0.525	0.59	2.03	1.35
Ferrite	0.475	1.46E-2	0.74	1.80

The results from simulation are compared with experiments in Fig. 3.4. In the simulation, longer holding times at T_{IA} result in a monotonic increase in the

volume fraction of austenite as the system reaches equilibrium. This state, however, is reached, even at these elevated temperatures, over a very long time (hundreds of days). This is not practical in real applications and we consider these calculations as the upper bound for the partitioning of the elements.

Experimental results are obtained from reference [97] as Fig. 3.5. The sample is heated up to 1223 K and processed 573 K through Equal Channel Angular Pressing (ECAP) twice to homogenize the structure. It is then cut into 8 mm x 3 mm x 1 mm for heat treatment. The samples are then subject to IA treatment corresponding to the simulations. Comparing with theoretical results (Fig. 3.6), the volume fraction of austenite changes dramatically with time. As mentioned, both heating rate and initial micro-structure affect the phase transformation during IA. In this sample, the grain size is small and more importantly the microstructure is more homogeneous. Actually, the homogeneous distribution of cementite causes the distribution of composition being more non-homogeneous. This is because the concentration of Mn and C in cementite is much higher than in ferrite (Table 3.3). The same situation for Si content which is much higher in ferrite then cementite. The interactions between species are more dramatic, which may affect the moving interface and the diffusion rate of the species. As a consequence, the evolution of the micro-structure during IA is not properly simulated by the present model.

Table 3.3: The equilibrium state of Fe-0.32C-1.42Mn-1.56Si at 300K (the composition is in -wt%)

	Vf	w_C	w_{Mn}	w_{Si}
Ferrite	0.95	6.56E-11	2.04E-4	1.64
Cementite	0.05	6.72	29.83	4.72E-11

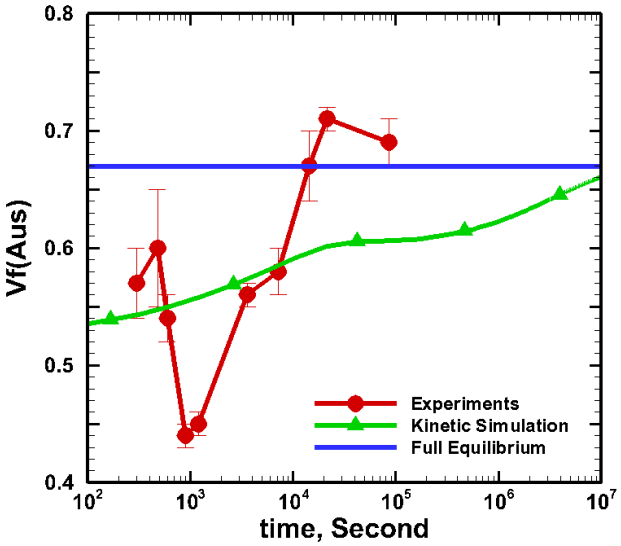

Figure 3.4: The transformation of austenite at T_{IA}=1045K as function of time; the experiments are done by R. Zhu

(a) 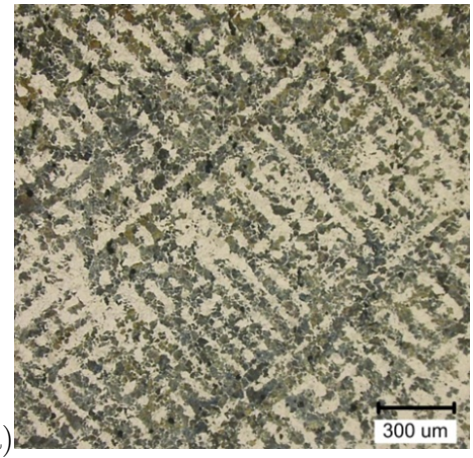

(b) 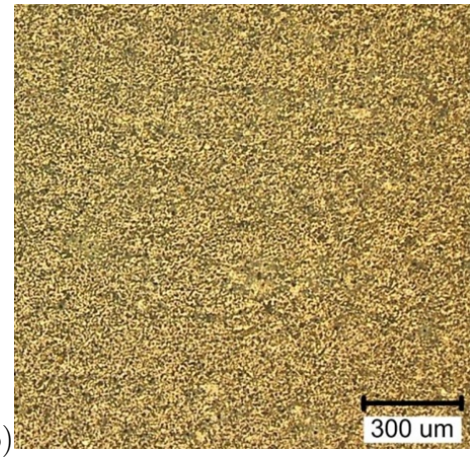

Figure 3.5: The optical microscopy images (a) before ECAP (b) after ECAP 2C processing [97]

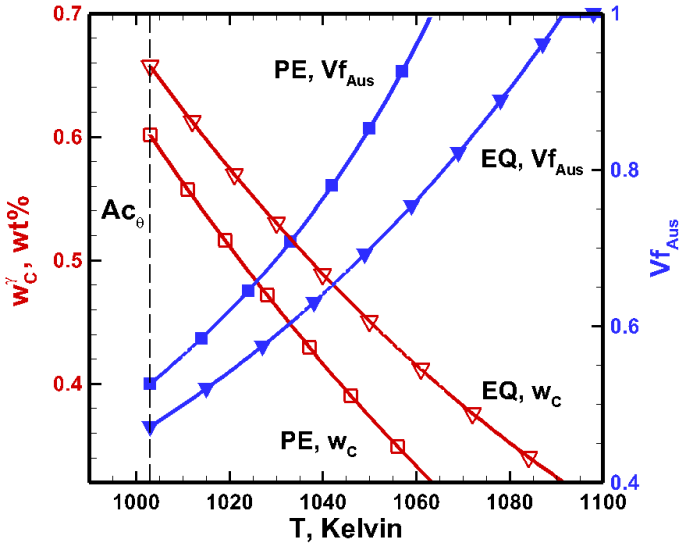

Figure 3.6: The predicted w_C^γ and volume fraction of austenite after IA under different conditions: EQ and PE are the predictions under equilibrium and para-equilibrium conditions

4. BAINITE ISOTHERMAL TRANSFORMATION

Thermodynamic calculations provide information to understand the thermodynamic state of the phases during BIT treatment. However, these calculations are always done under the assumption of homogeneity in the microstructure, which in turn achieves equilibrium. In this chapter, the kinetic models are also introduced to describe the time dependent micro-structure evolution and the diffusion of the alloying elements.

4.1 Bainite Isothermal Transformation

In order to to allow the transformation of IA austenite into bainite, the isothermal holding temperature (T_{BIT}) must be higher than the martensitic start temperature (T_{Ms}) of the IA-austenite and must be lower than the bainite start temperature (T_{Bs}). Since IA-ferrite is stable below Ac_1 [44], the thermodynamic analysis for BIT treatment can be carried out by considering only IA-austenite, with its chemical composition corresponding to that at the end of IA (point (1) in Fig. 1.1). Within this temperature range, carbon is proposed to diffuse into austenite under para-equilibrium condition during bainitic nucleation (para-equilibrium means only carbon can diffuse across the interface in this case). In contrast to the bainite nucleation process, the growth rate of the bainite subunits is very fast and it is assumed to occur in a diffusionless fashion. [13]

Despite existing uncertainties regarding the specific mechanisms for the bainitic transformation, extensive work by Bhadeshia and others suggest that the bainitic transformation is only thermodynamically possible when (1) the maximum driving force ($\triangle G_{Max}$) overcomes the so-called universal nucleation energy ($\triangle G_N$)and (2) the diffusionless driving force ($\triangle G^{\gamma\rightarrow\alpha}$) is greater than stored energy ($\triangle G_{SE}$) [12].

These two conditions are illustrated in Fig. 4.1.

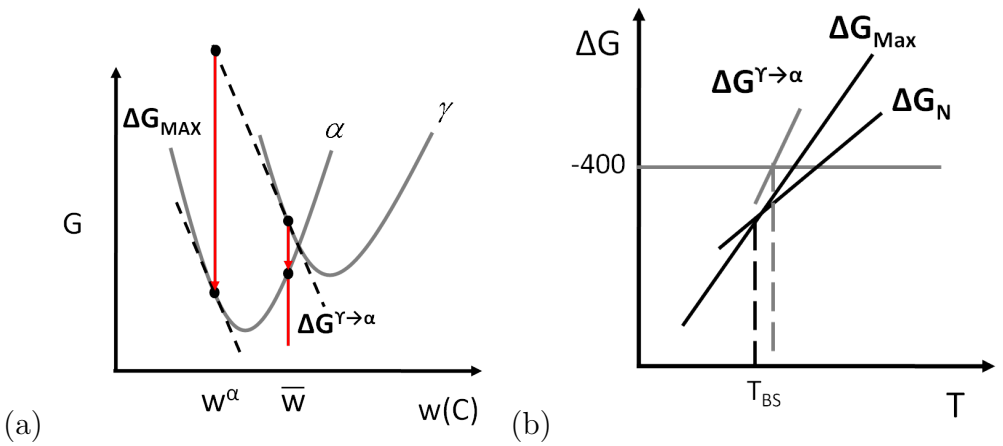

Figure 4.1: The schematic diagram for estimating the driving force for BIT[12]: ΔG_{MAX} is the maximum driving force for the nucleation of the bainite; $\Delta G^{\gamma\rightarrow\alpha}$ stands the diffusionless driving force; in order to initiate the bainitic transformation, the maximum driving force must be higher than the nucleation energy (ΔG_N); the $\Delta G^{\gamma\rightarrow\alpha}$ must be lower than -400 J/mol to keep the growing process

The universal nucleation energy is essential for the prediction of T_{Bs}. However, this ΔG_N is an empirical quantity which was determined by comparing experimentally determined T_{Bs} with the chemical driving force for the bainitic transformation obtained from thermodynamic calculations using specific thermodynamic databases. In previous work, it was reported as $\Delta G_N = 3.637(T - 273.18) + 2540$ [2, 67].

Unfortunately, if one is to use these ideas with different thermodynamic databases, it is necessary to adjust this function. In this work, this quantity is re-fitted by using the Thermo-Calc database TCFE6 (V6.2) (as Fig. 4.2(a)), and obtained the following function:

$$\Delta G_N = 4.736T - 4769 \tag{4.1}$$

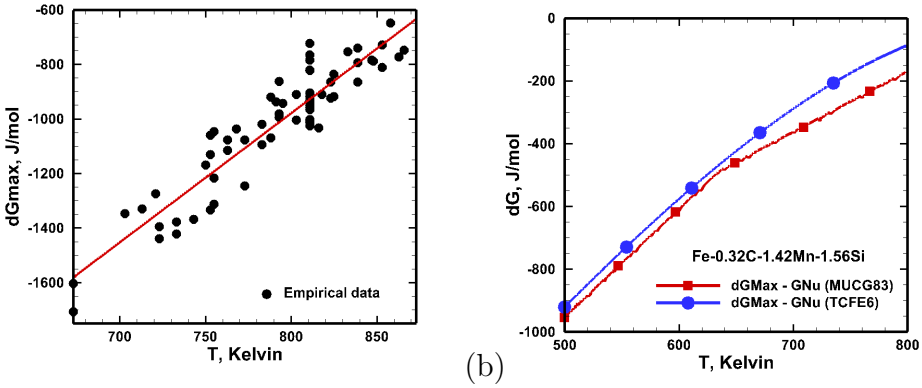

Figure 4.2: (a) The fitting curve for universal nucleation based on TCFE6 database; the empirical data is obtained from [19, 96]; (b) the effective driving force

In order to predict the thermodynamic stability limit for the formation of bainite one must also calculate the maximum chemical driving force for the formation of bainite, which is given by [9]:

$$\Delta G_{Max} = RTln(\frac{a(w^{\alpha}_{Fe})}{a(w^{\gamma}_{Fe})}) \tag{4.2}$$

where $a(w^{\alpha}_{Fe})$ and $a(w^{\gamma}_{Fe})$ are the Fe chemical activities in bainitic ferrite under para-equilibrium conditions (considering only the partition of C) and the carbon content in austenite is corresponding to the instantaneous composition of the austenite matrix.

To verify that the calculations yield the quantitative results, the effective driving force $(\Delta G_{Max} - \Delta G_N)$ calculated using the updated universal nucleation energy and the chemical driving forces calculated using Thermo-Calc and compare it with the results obtained using the MUCG83 code as Fig. 4.2(b).

If one assumes that the growth of bainite plates occurs in a partitionless fashion, then the available chemical driving force for the transformation is given by the Gibbs free energy difference between austenite and ferrite $G^{\gamma} - G^{\alpha}$ at the instantaneous

composition of the austenite matrix.

As the bainitic transformation progresses, this driving force starts to decrease with the composition change until it vanishes completely. This critical composition as a function of temperature is denoted as T_0. The transformation of austenite into bainite also requires overcoming a mechanical energy barrier associated to the mechanical interactions between the growing bainite plate at the expense of the austenite matrix. This so-called stored energy ($\triangle G_{SE}$) is the energy necessary to support the shape deformation as bainite is forming and has been estimated by Bhadeshia to be about -400 J/mol [12]. As the transformation progresses, carbon is ejected from the growing bainite and enriches the residual austenite. With the increasing carbon content in untransformed austenite, the diffusionless driving force is decreasing until it equals the stored energy. This thermodynamic constraint to the bainitic transformation is denoted as T_0'.

4.2 Martensitic Transformation (T_{Ms}, T_{Mf})

Depending on the chemical composition and heat treatment, Martensite may occupy 1% to 5% total volume of TRIP steel [55]. In the present alloy, the further carbon partitioning from martensite into austenite is not considered and the design of the heat treatments is developed around the idea of minimizing the formation of martensite, through the control of the IA and BIT treatment parameters.

In the two-step heat treatment investigated in this work, martensite may form after rapid quenching to BIT (point (2) in Fig. 1.1) or after quenching from BIT to room temperature (point (4) in Fig. 1.1). In other words, if T_{BIT} is higher than T_{Ms} after IA ($T_{BIT} > T_{Ms,1}$) and T_{Ms} after BIT is lower than room temperature ($T_{Ms,2} < 300K$), martensitic transformation can be avoided.

Although there are many models being built to predict T_{Ms} [42, 40, 35, 24], in

this work, a thermodynamics-based model is implemented: the free energy barrier ($\triangle G_{Ms}$) to martensitic transformation is in the range of 1100 to 1400 J/mol while the molar fraction of carbon is between 0.01 to 0.06 [8] and in this case, we can estimate T_{Ms} by calculating the diffusionless driving force:

$$\Delta G^{\gamma \to \alpha} < \Delta G_{Ms} \tag{4.3}$$

Fig. 4.3 compares the martensite start temperature (T_{Ms}) using different approaches, including the calculations using the thermodynamic arguments described in Eq. 4.3. The figure shows that the thermodynamic model provides lower austenite stability than Andrew's model [5, 87] and close to Ishida's model [42].

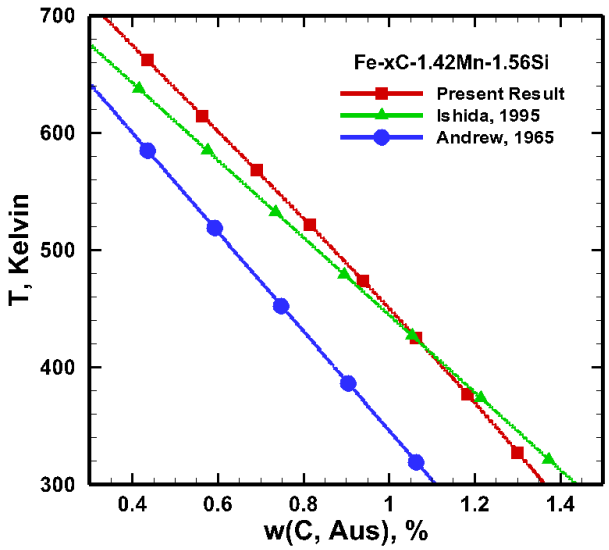

Figure 4.3: The predicted martensite start temperature of Fe-0.32C-1.42Mn-1.56Si [42, 5]

Due to the diffusionless nature of martensite, the volume fraction of martensite

at arbitrary temperatures below T_{Ms} is calculated using the K-M relation [50, 21]:

$$V_{fM} = 1 - exp[-0.011(T_{Ms} - T)] \tag{4.4}$$

Compared to bainite or ferrite, martensite possesses higher carbon content. This means that the formation of martensite can lower the carbon enrichment of austenite and reduce its stability against martensitic transformation upon cooling from T_{BIT} to room temperature. As mentioned above, the formation of the martensite can be avoided by heat treatments. As shown in Fig. 4.4, if T_{BIT} is higher than $T_{Ms,1}$, Vf(Mar,1) is, in principle, zero. If carbon content is higher than w^{273}, the austenite will be retained at 0 ^{o}C. In this case, there is no martensite while the alloy is at temperatures above 0 ^{o}C. The red triangle in Fig. 4.4 constitutes the optimum area in which the formation of martensite can be suppressed and constitutes the ideal design window for the selection of the heat-treatment temperatures.

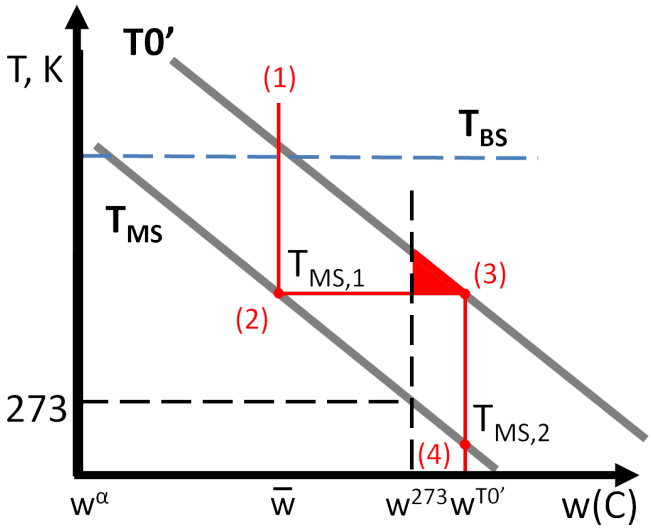

Figure 4.4: The schematic diagram for precluding martensitic transformation at optimum T_{BIT}

We would like to note that the existence of this martensite-free design window is not guaranteed for an arbitrary alloy composition. Based on the full equilibrium calculation while T_{IA}=1045 K, the chemical composition is Fe-0.47C-1.76Mn-1.42Si in austenite. According to the described model, the phase diagram for BIT is calculated as Fig. 4.5. In this case, in order to avoid the formation of the martensite after IA, T_{BIT} should be higher than 649 K; on the other hand, it needs to be lower than 485 K in order to guarantee sufficient enrichment of austenite to stabilize it against martensitic transformation upon quenching to room temperature. It is obvious that, in this alloy, it is impossible to suppress the martensitic transformation after this IA treatment. Neither do the cases with T_{IA} is 1023 or 1083 K as shown in Fig. 4.6 (the inputs for phase diagram are as Table 4.1). This means the red triangle in Fig. 4.4 does not exist and martensitic transformation can not be avoided based on thermodynamic calculations.

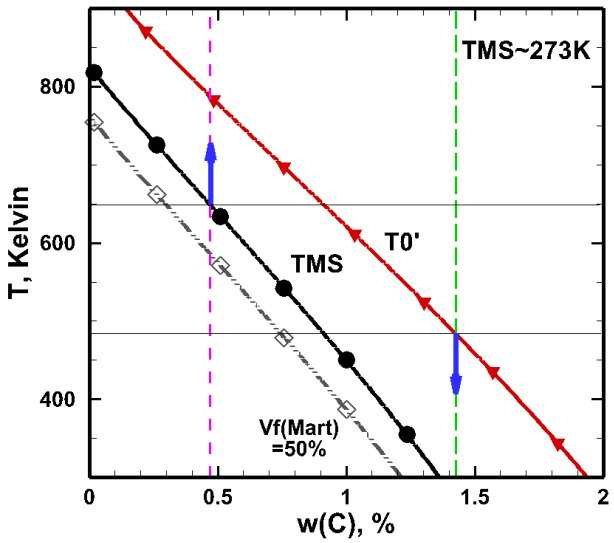

Figure 4.5: The calculated phase diagram for BIT as T_{IA}=1045K

Table 4.1: The equilibrium composition of Fe-0.32C-1.42Mn-1.56Si alloy at different T_{IA}s

	w(C)	w(Mn)	w(Si)
T_{IA}=1023 K	0.56	1.96	1.36
T_{IA}=1045 K	0.47	1.76	1.42
T_{IA}=1083 K	0.34	1.53	1.48

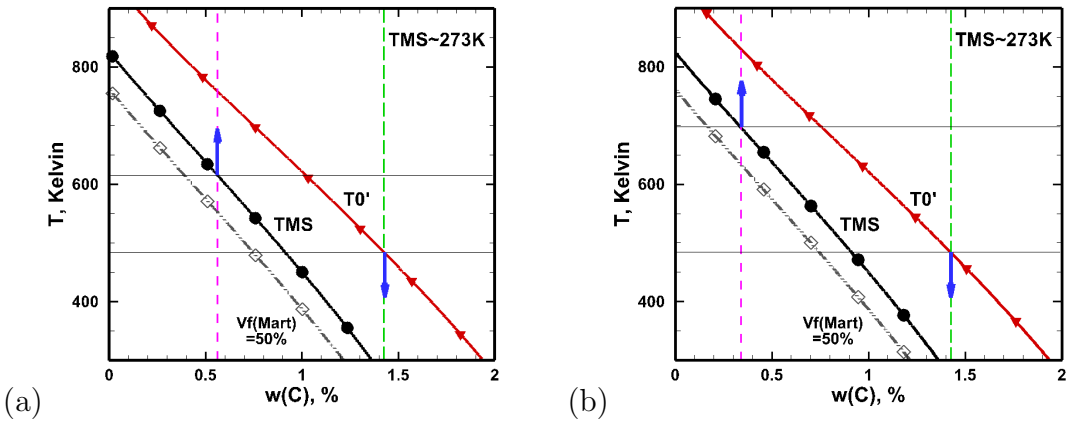

Figure 4.6: The phase diagram for BIT while (a) T_{IA}=1023K (b) T_{IA}=1083K

4.3 Application of the Thermodynamic Analysis to Experiments

As discussed in chapter III, the system is not properly simulated by the present theoretical model and thermodynamic analysis provides only a limiting case for the expected phase constitution after IA. In order to approach the full equilibrium state in experiments, two hours holding for IA is tested and six sets of conditions for experiments are listed as Table 4.2 and 4.3. The heat treated time for BIT is estimated by diffusion controlled model [76, 77] which is introduced in the coming chapter.

Table 4.2: The empirical results from different heat treatments [61]

Treatment	A	B	C	D
IA	1023 K, 2 hrs	1045 K, 2 hrs		
BIT	613 K, 12 mins	613 K, 15 mins	643 K, 15 mins	693 K, 5 mins
Vf(Aus)	11.73 ± 2.5%	11.85 ± 3.04%	18.61 ± 1.54%	20.40 ± 1.84%
Vf(Fer)	-	41.20 ± 0.8%		
w^{γ}_{Mn}	-	1.48		
w^{γ}_{Si}	-	1.49		
w^{γ}_{C2}	-	1.12	1.22	1.21

Table 4.3: The empirical results from different heat treatments - continued [61]

Treatment	E	F
IA	1083 K, 2hrs	1045 K, 10 mins
BIT	613 K, 15 mins	613 K, 15 mins
Vf(Aus)	7.37 ± 1.04%	11.56 ± 3.25%
Vf(Fer)	15.10 ± 0.5%	52.70 ± 3.0%
w^{γ}_{Mn}	1.5	1.40
w^{γ}_{Si}	1.43	1.70
w^{γ}_{C2}	1.29	1.09

4.3.1 Different T_{IA}, Constant T_{BIT}

According to Table 4.2, in treatment A, B and E, three different IA temperatures, 1023, 1045 and 1083 K, are applied while T_{BIT} is fixed at 613 K. As mentioned above, the thermodynamic predictions in Fig. 4.7(a) shows about 50% error comparing with experimental results. The discrepancy is blamed to the competition between carbon diffusion and phase transformation during BIT[90]. It is indicated that the carbon enrichment in retained austenite is actually closer to the T_0 curve in phase diagram instead of T'_0 [82, 44, 43].

The results show that the T_0 criterion agrees well with experiments *if one considers that the thermodynamic limit to the bainitic transformation is actually* T'_0. Of course, if one takes into account the mechanical barrier to the growth of austenite, and if one accepts the diffusionless nature of the bainitic transformation, this implies

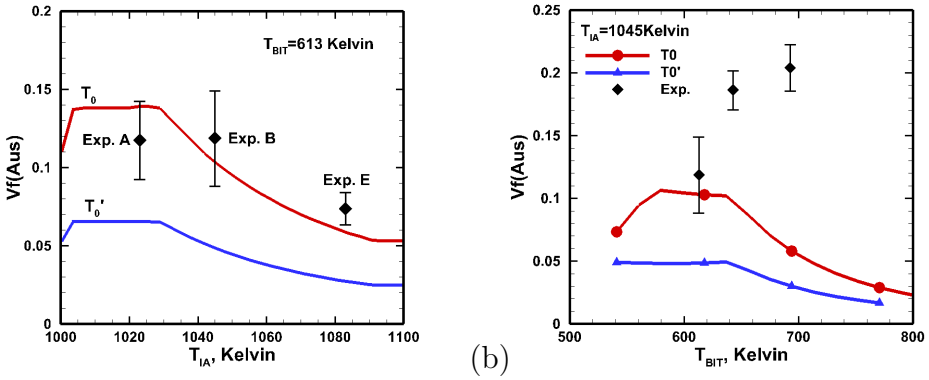

Figure 4.7: The volume fraction of retained austenite after two-step heat treatment (a) the same T_{BIT} and different T_{IA} (b) the same T_{IA} and different T_{BIT} [61]

that the transformation progresses even if the thermodynamic driving force is exhausted or actually is negative, which is impossible from the thermodynamic stand point. In the next chapter, further analysis of this process will be carried out and it will be shown how the apparent controversy can be resolved.

4.3.2 Different T_{BIT}, Constant T_{IA}

Schedules B, C and D correspond to treatments with the same T_{IA} at 1045 K and T_{BIT} at 613, 643 and 693 K. As shown above in Fig. 4.7(b), the use of T_0' or T_0 as the thermodynamic limit for the bainitic transformation is not consistent does with the experimentally determined volume factions of austenite. For each treatment, the observed amount of retained austenite is higher than the predicted one with dramatic qualitative differences with respect to the experimental observations. This discrepancy suggests that the carbon content in austenite after IA and BIT must be significantly higher than what one would predict using the thermodynamic approach.

4.4 Reverse Calculation

Experiments shown in Fig. 4.7(b) suggest that the carbon enrichment of the retained austenite after BIT is higher than what one would predict based on the thermodynamic limit (T_0'/T_0). In this section, this possibility is investigated: at the same time the thermodynamic model is used by combining thermodynamic analysis along with experimental observations. This approach is termed as 'reverse calculation' because we are trying to solve an inverse problem: *given some experimental information about the state of the alloy after BIT and IA, what is the likely evolution of carbon in order to be consistent with experiments.* Essentially, we propose to use this approach to estimate the carbon content in austenite before and after BIT, using the following input from experiments: (1) volume fraction of retained austenite (Vf(Aus,4)), (2) volume fraction of inter-critical ferrite (Vf(Fer)), weight fraction of (3) manganese (w^{γ}_{Mn}) and (4) silicon (w^{γ}_{Si}) in austenite after IA. The reader is referred back to Fig. 1.1(a).

1. The first step in this approach is to guess the weight fraction of carbon in retained austenite ($w^{\gamma}_{C,2}$) after BIT. With this estimate and the inputs from experiments, $T_{Ms,2}$ can be predicted by using Eq. (4.3). If $T_{Ms,2}$ is higher than room temperature (300 K), the martensitic transformation is expected upon the cooling from T_{BIT} to room temperature. The volume fraction of martensite generated at this step is predicted as:

$$\frac{Vf(Mar,2)}{Vf(Mar,2)+Vf(Aus,4)} = 1 - exp[-0.011(T_{Ms,2} - 300)] \qquad (4.5)$$

2. The second step is to guess is the weight fraction of carbon in austenite before the BIT treatment ($w^{\gamma}_{C,1}$) which is at stage (2) in Fig. 1.1(a). The calculation

is similar to the first step, Vf(Mar,1) can be estimated by Eq. (4.4).

3. With these calculations, the volume fraction of bainite can be presented as:

$$Vf(Bai) = 1 - Vf(Fer) - Vf(Mar,1) - Vf(Mar,2) - Vf(Aus,4) \quad (4.6)$$

4. Applying the lever rule with the supposed carbon concentrations before and after BIT ($w^{\gamma}_{C,1}$ and $w^{\gamma}_{C,2}$), the volume fraction of bainite can also be calculated as: [67]

$$Vf(Bai) = \frac{w^{\gamma}_{C,2} - w^{\gamma}_{C,1}}{w^{\gamma}_{C,2} - w^{para,\alpha}_{C}} \quad (4.7)$$

where $w^{para,\alpha}_{C}$ is the carbon concentration in bainite under para-equilibrium condition.

5. By using Eq. (4.6) and (4.7), the corresponding set of $w^{\gamma}_{C,1}$ and $w^{\gamma}_{C,2}$ can be found at T_{BIT}.

4.4.1 Validation

In order to verify this 'reverse thermodynamic analysis', the conventional 'forward' calculation is used as control. For this forward calculation, T_{IA} and T_{BIT} are chosen as 1003 K and 528 K, respectively. In the reverse calculation, there are two inter-dependent austenite carbon compositions, corresponding to the state of the alloy before and after BIT. For a given 'guess' for the carbon content in austenite at the end of BIT there will be a corresponding carbon concentration in IA-austenite. This approach is illustrated in Fig. 4.8.

One of the results of this reverse analysis corresponds to a state with 15.4% volume of bainite, which is close to the prediction by forward calculation. Comparing Vf(Mar), $w^{\gamma}_{C,1}$ and $w^{\gamma}_{C,2}$, the relative error being less than 1%. The results are listed

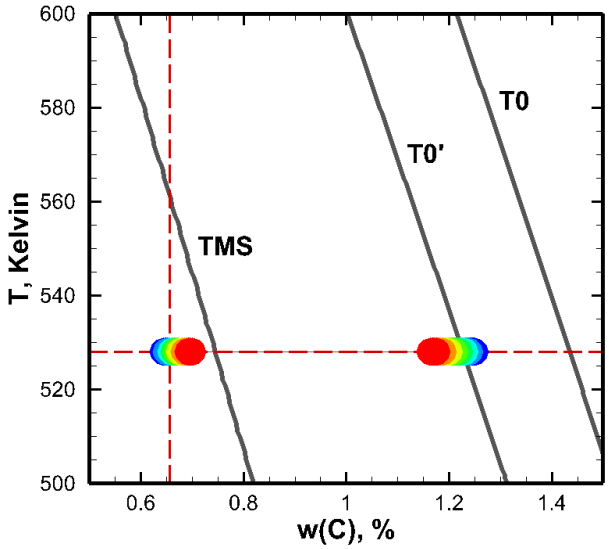

Figure 4.8: The paired results obtained by reverse calculations; (T_{IA}=1003 K, T_{BIT}=528 K)

in Table 4.4.

According to the forward calculation in Table 4.4, $w^{\gamma}_{C,1}$ under equilibrium condition at 1003 K is 0.656 wt% and the manganese and silicon contents in austenite are about 2.18 and 1.32 wt%. On the other hand, the inter-critical ferrite occupies 52.9% of the total volume. If the maximum carbon content in retained austenite meets the T'_0 curve, at 528 K, $w^{\gamma}_{C,2}$ should be about 1.227 wt%. According to lever rule and K-M relation (Eq. (4.4), and (4.7)),the martensite and bainite should take 20.1% and 15.3% of total volume respectively, while the volume fraction of the retained austenite is about 11.7%. Comparing to forward calculation, reverse calculation provides all the possible cases to interpret the observations in experiments. This helps to understand the carbon diffusion through the heat treatment.

We now apply the reverse calculation to examine treatments B and E in Table 4.2:

Table 4.4: The predicted state of the product alloy (T_{IA}=1003 K, T_{BIT}=528 K)

	Vf(Mar)	Vf(Bai)	$w^{\gamma}_{C,1}$	$w^{\gamma}_{C,2}$
Forward	0.201	0.153	0.656	1.227
Reverse	0.200	0.154	0.659	1.227

1. After treatment B, $w^{\gamma}_{C,2}$ is in the range of 1.14 wt% to 1.22 wt% by reverse calculation and 1.12 wt% by XRD measurement [97]. The corresponding $w^{\gamma}_{C,1}$ should be within 0.53 to 0.63 wt% in order to be consistent with the observed enrichment. This enrichment of IA-austenite is only possible if the alloy does not achieve full equilibrium after IA. As mentioned above, this is exactly the case when using IA treatment times in the order of minutes to hours [97] with T_{IA} in the order of 1045 K. Even in the case of the alloy treated for 2 hours, the composition is still far away from equilibrium at 1045 K.

2. On the other hand, in the case of treatment E, $w^{\gamma}_{C,2}$ is 1.29 wt% by XRD. Using the reverse calculation, if $w^{\gamma}_{C,2}$ is 1.29 wt%, the corresponding $w^{\gamma}_{C,1}$ is 0.358 wt%. This predicted value is close to 0.343 wt% which corresponds to the equilibrium state at 1083 K. With this low carbon content, martensite forms during quenching process after IA. Therefore, Vf(Mar,1) in treatment E is larger than in treatment B because of $w^{\gamma}_{C,1}$. Even at the same T_{BIT}, treatment E results in significantly more martensite than B. This is the reason why the treatment E makes higher carbon enrichment but lower volume of retained austenite.

3. From the analysis of these two treatments, it is evident that the closer the alloy is to equilibrium the less carbon is dissolved in austenite. On the other hand, under non-equilibrium conditions significant further enrichment of IA-

austenite can be achieved. This observation is validated by analyzing another experiment, labeled as F in Table 4.2. In treatment F, the alloy is inter-critical annealed for 15 mins at 1045 K. The predicted $w^{\gamma}_{C,1}$ is 0.55 wt% and Vf(Mar,1) is zero. According to the time scale in Fig. 3.4, the alloy requires over 115 days to achieve full equilibrium. It explains why two hours treatment at 1045 K (treatment B) does not make obvious difference with 15 mins (treatment F) when it comes to the amount of retained austenite after BIT.

In the treatment schedules labeled as B, C and D, the alloy samples are treated using the same IA treatment, so, the chemical composition is ideally identical and it is very likely that the composition of austenite after IA is also quite similar. Using the experimental inputs described above, the most likely combinations of carbon content in austenite before and after BIT are shown in Fig. 4.9.

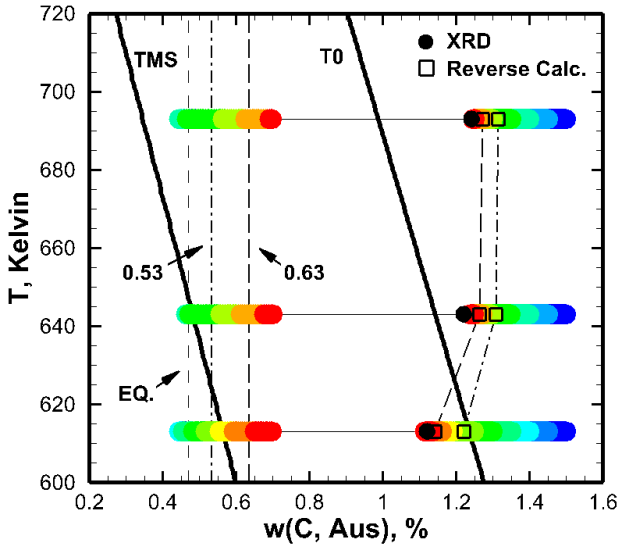

Figure 4.9: The reverse calculations while T_{IA}=1045 K comparing to the experiments

In the case of treatment B, the most likely composition of IA-austenite $w^{\gamma}_{C,1}$ is 0.53 wt%, while in the case of treatment C, this composition is closer to 0.63 wt%. While there is obviously some uncertainty in the calculations, it is evident that $w^{\gamma}_{C,1}$ lies within the 0.53 to 0.63 wt% range after 2 hours at 1045 K. This is significantly higher than the expected IA-austenite carbon composition under equilibrium conditions, but it is consistent with a reduced volume fraction of austenite reported in [97].

More importantly, Fig. 4.9 shows that either using the 'reverse analysis' or XRD measurements, one can conclude that $w^{\gamma}_{C,2}$ must be larger than T_0. This is perhaps the reason why the forward calculation under-estimates the volume fraction of retained austenite. From this analysis, $w^{\gamma}_{C,1}$ is about 0.06 to 0.16wt% larger than the thermodynamic limit. This enrichment suppresses the formation of martensite during the quenching process. This explains why in treatment B, even though $w^{\gamma}_{C,2}$ is less than T_0, the volume fraction of retained austenite can be larger than the prediction based on using the thermodynamic approach.

Fig. 4.9 shows that in treatments C and D, the carbon enrichment in retained austenite is beyond T_0 curve. It is reported that this super-enrichment of retained austenite is the result of competition between the bainitic transformation and carbon diffusion in austenite [90, 34]. This is discussed in the coming chapter.

In the following chapter it will be shown as Fig 4.10 how we can examine the bainitic transformation using an improved description that takes into account the heterogeneous distribution of carbon in the retained austenite as the bainitic transformation progresses.

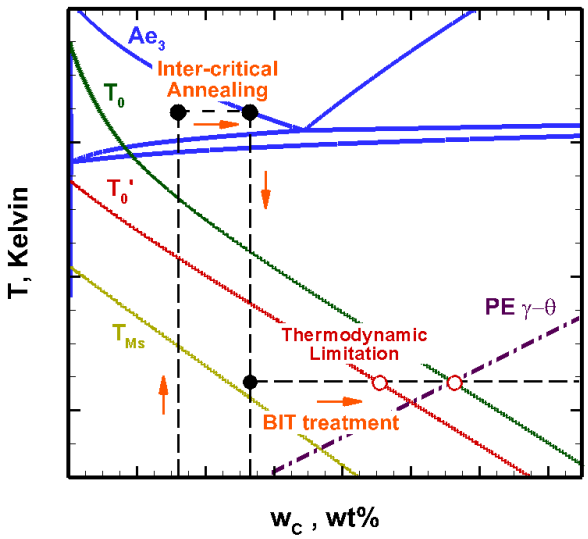

Figure 4.10: The schematic diagram of the heat treatment to suppress the formation of cementite

5. THE KINETIC MODEL FOR BAINITE ISOTHERMAL TRANSFORMATION

From experimental work performed over the past decades, it has become obvious that during the bainitic transformation, particularly when it occurs at relatively low temperature, if there is mass diffusion at all, it must involve almost exclusively carbon. This is because the phase transformation rate is much higher than the diffusion of the substitutional elements. In fact, the bainitic transformation can be considered to be a "displacive transformation" [13]. On the other hand, competing explanations for the bainitic transformation suggest that the transformation is actually controlled by diffusional processes at the bainite/austenite interface. Such processes even include redistribution of the substitutional elements. There is thus still a very active debate regarding the dominant driving forces for the motion of the bainite/austenite interface. In this chapter, we examine some of the models proposed to describe the transformation. We then propose an alternative model that resolves some of the paradoxical results obtained in the experiments.

For estimating the transformation time, a certain amount of empirical or fitting parameters are always required for all the models. This may cause some accuracy issues whenever the chemical composition or the environment for experiments are changed. Solving this problem is not the purpose of this work; on the other hand this work is focused on investigating the mechanisms by which the alloys studied in the experiments exhibit (performed by our experimental counterparts in Dr. Karaman's group) enrichments that go beyond the thermodynamic limits corresponding to T_0 or T_0'.

5.1 Displacive Transformation Model

Some models for bainitic transformation are based on the idea that suggests that the phase transformation (nucleation and growth of the bainite subunit) occurs prior to carbon diffusion [78, 79, 33, 34]. In other words, the bainite sub-unit grows with high carbon content in a very short time and carbon is repelled from bainite to austenite after the bainite subunit finishes the growth process. In these models, the nucleation process consumes most of the time for bainitic transformation [34].

As the driving force overcomes the nucleation energy, the transformation is triggered. In the previous chapter, the universal nucleation energy is modified, corresponding to TCFE6 (V6.2) database as Eq. 4.1. Following Jacques' model [34], the transformation criterion is presented as:

$$F = tanh(-\frac{\Delta G_m - G_N}{RT}),\ while\, |\Delta G_{Max}| > |G_N| \tag{5.1}$$

ΔG_{Max} is the maximum driving force which is the same as 4.2.

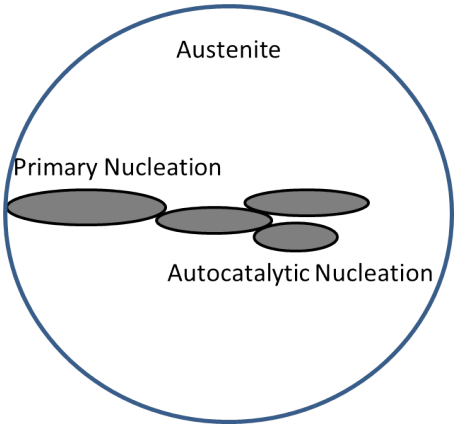

Figure 5.1: The schematic diagram for bainitic transformation

As shown in Fig. 5.1, while the driving force is sufficient to drive the bainitic transformation, the bainite sub-unit nucleates at the austenite grain boundary and this is indicated as primary nucleation. The number of nuclei forming during the time interval $d\tau$ is approached by [34]:

$$dI_P = N_0 \cdot s_\gamma \cdot \nu \cdot F \cdot d\tau \tag{5.2}$$

N_0 is the surface density of the potential nucleation site which is fitted as $2 \times 10^{-4} nuclei \cdot m^{-2}$ to experiments. s_γ is the remaining austenite grain boundary area, which is a function of the austenite grain size ($\overline{L}$) and volume fraction of residual austenite (v_γ) [34, 67]:

$$s_\gamma = \frac{2}{\overline{L}} \cdot v_\gamma^{\frac{2}{3}} \tag{5.3}$$

In this model, it is assumed that the bainite sub-unit is in lenticular shape. It is reported that the aspect ratio of the bainite sub-unit is about 0.025 [88] and the thickness can be approached by empirical formula $t_B = 2.0 \times 10^{-7} \times (T - 528)/150$ [67]. The volume of bainite sub-unit can be presented as: (m^3)

$$V_{UB} = 3.2 \times 10^{-18} \pi \times (\frac{T - 528}{150})^3 \tag{5.4}$$

More bainite may nucleate on top of these primary sub-units. This corresponds to the so-called auto-catalytic nucleation process. It is related to the primary nucleation rate, the diameter of the austenite grain (D_γ), the length of a single bainite sub-unit (l_B), and effective driving force. This process is formulated as:

$$dI_a = \beta_a \cdot I_P \cdot \frac{2D_\gamma}{\pi \cdot l_B} \cdot F \cdot d\tau \tag{5.5}$$

where β_a is the other fitting parameter. According to Avrami's extended volume correction, the change of the bainite volume is

$$dV_B = V_\gamma \cdot (I_P + I_a) \cdot V_{UB} \cdot exp(-\frac{\triangle G^{\gamma\to\alpha}}{RT}) \cdot d\tau \tag{5.6}$$

V_γ is the volume of the residual austenite and $\triangle G^{\gamma\to\alpha}$ is the diffusionless driving force which allows austenite transforming into bainite.

In this model, most of the parameters can be obtained by CALPHAD method with a proper database but three parameters, i.e. the size of bainite sub-unit (V_{UB}), the potential nucleation site (N_0) and β_a. The size of bainite sub-unit is decided by empirical formula which is a statistical result; more importantly, the two fitting parameters, N_0 and β_a are not adjusted in this work.

5.2 Austenite Film

Following the bainitic transformation, carbon is repelled from bainite sub-unit and diffusing into residual austenite under para-equilibrium condition. As more bainite is generated, austenite receives more carbon which decreases the driving force for the bainitic transformation and this slows down the transformation rate. If carbon diffuses without any constrains and distributes homogeneously in austenite, bainitic transformation stops while austenite reaches the so-called T_0' curve [16]. This corresponds to the so-called thermodynamic limitat for BIT. However, there are many issues causing the non-homogeneous carbon distribution:

Firstly, carbon diffusion in austenite, while fast, is actually finite in nature and it does not occur faster than other phenomena associated to the formation and growth of the bainite sub-unit. Because of the difference of carbon diffusion rate between bainitic ferrite and austenite, it is usually postulated that carbon escapes bainite in a fast manner, but accumulates in the austenite matrix immediately adjacent to the

austenite/bainite interface. At the initial stage of BIT, high carbon concentration at interface on the austenite side (w_C^{γ}) leads to the formation of a thin-film-like carbon-rich austenite phase [20, 54]. The growing bainitic ferrite plate also produces the austenite film and impedes further carbon diffusion. Theoretically, in austenite, the "local" position with lower carbon concentration possesses higher driving force for bainitic transformation which stands higher probability of nucleation. Carbon diffusion is constrained between bainitic ferrite plates and does not contribute to the phase transformation. Therefore, more bainitic ferrite plates are allowed to form and the "average" carbon content in retained austenite is higher than the thermodynamic limitation. This is the reason why T_0' prediction does not match the experiments.

Because the location of a particular nucleation event is highly dependent on the micro-structure and the local nucleation driving force, the prediction of the kinetics of the bainitic transformation is highly challenging. In order to predict the maximum carbon content in retained austenite, some assumptions are postulated: (1) Carbon diffuses only in $+x$ direction, that is, the direction perpendicular to the major axis of the bainite sub-unit. Because the aspect ratio is high, the carbon diffusion in the other direction is neglected. (2) Carbon diffusion in austenite stops while bainite finishes growing. Under this assumption, austenite films possess maximum carbon concentration in a minimum volume. (3) Within the austenite film, the volume with the carbon content less than $w_C^{T_0'}$ can in principle transform into bainitic ferrite. So, it is assumed that the carbon content in the range between $\overline{w}_C$ to $w_C^{T_0'}$ in the film goes to the residual austenite. The carbon content out of the austenite film corresponds to the average of the low carbon content film and residual austenite. (4) The next bainite sub-unit generates the film right at $w_C^{T_0'}$; therefore, carbon is constrained between bainitic ferrite plates.

As shown in fig. 5.2, the maximum average carbon content in retained austenite

is proposed under these four assumptions.

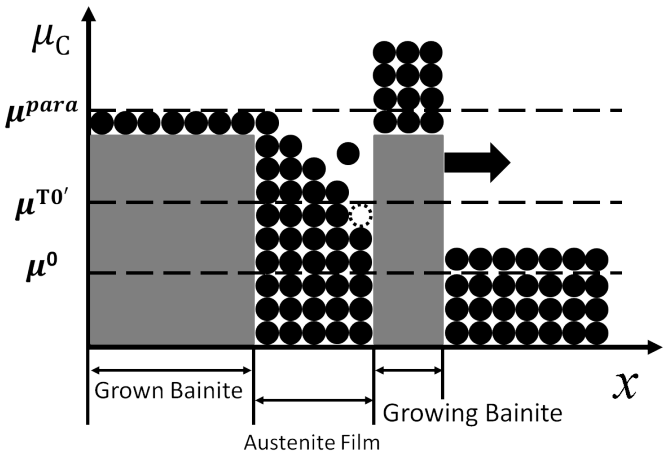

Figure 5.2: The schematic diagram for ideal BIT

In order to estimate the stability of the retained austenite, it is important to know the carbon concentration in austenite film. Since carbon diffusion across the bainite-austenite interface can be approached by para-equilibrium condition, the carbon distribution can be presented by Fick's second law. One of the analytical solution is approached by employing the dimensionless parameter and obtaining the concentration profile as[39, 72, 7, 20]:

$$w(x,t_d) = \overline{w} + (w^{\gamma\alpha} - \overline{w}) erfc[\frac{x}{2(\overline{D}t_d)^{0.5}}] \tag{5.7}$$

$\overline{w}$ and $w^{\gamma\alpha}$ are the carbon content in residual austenite and at interface on austenite side. $\overline{D}$ is the average carbon diffusion coefficient and t_d is the time for decarburizing the bainitic ferrite plate. This equation can not only be applied to calculate the carbon concentration in austenite film, but also for estimating t_d. At temperature T,

the thickness (t_B) of the bainitic ferrite plate can be estimated by empirical formula and the radius is close to $40t_B$. By integrating Eq. (5.7), t_d can be obtained.

$$t_d = \frac{\pi}{16\overline{D}}\left(\frac{t_B(\overline{w} - w^{\alpha\gamma})}{w^{\gamma\alpha} - \overline{w}}\right)^2 \tag{5.8}$$

Another approach is made by solving Fick's second law through the use of the finite difference method. Because carbon diffusion occurs after the bainite growth, the movement of the interface is neglected. The governing equation is translated into the difference equation:

$$w(x, t + \Delta t) = w(x, t) + \frac{\overline{D}\Delta t}{\Delta x^2}[w(x + \Delta x, t) - 2w(x, t) + w(x - \Delta x, t)] \tag{5.9}$$

When the amount of carbon in austenite film equals to the change in the carbon concentration in the bainitic ferrite plate, the decarburizing of bainitic ferrite is finished.

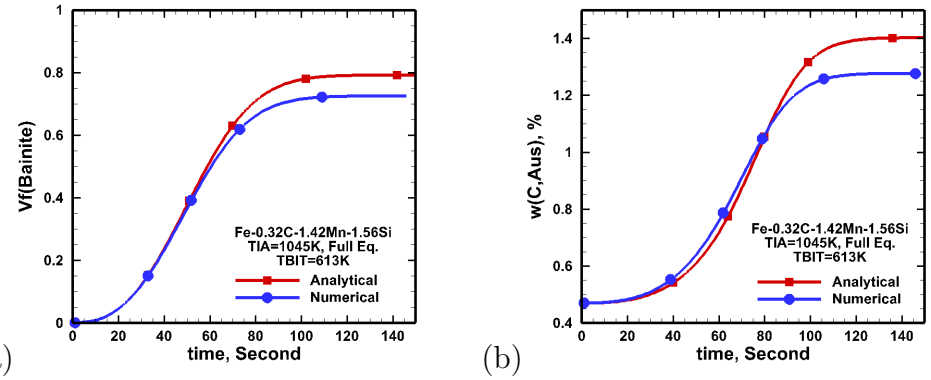

(a) (b)

Figure 5.3: The CCT diagram for bainitic transformation at 613 K, (a) the volume fraction of bainitic ferrite (b) the average carbon content in retained austenite as functions of time [62]

To test the model, the treatment B in Table 4.2 is examined. The alloy is initially inter-critically annealed at 1045 K and achieves the equilibrium state later. Fig. 5.3 compares the analytical solution with the numerical one. Along with the increasing of bainitic ferrite, carbon gradually enriches austenite. It is obvious that the analytical solution predicts higher w_{C2}^{γ} as well as a higher bainitic ferrite volume. This also corresponds to the decarburizing time calculated as Fig. 5.4. Because the average carbon content out of austenite film ($\overline{w}_C$) is increasing with bainitic ferrite volume, t_d which is calculated by Eq. (5.8) is also increasing. As Fig. 5.4, the numerical solution predicts more decarburizing time than the analytical solution. With more diffusion time, the average carbon content in the film is lower.

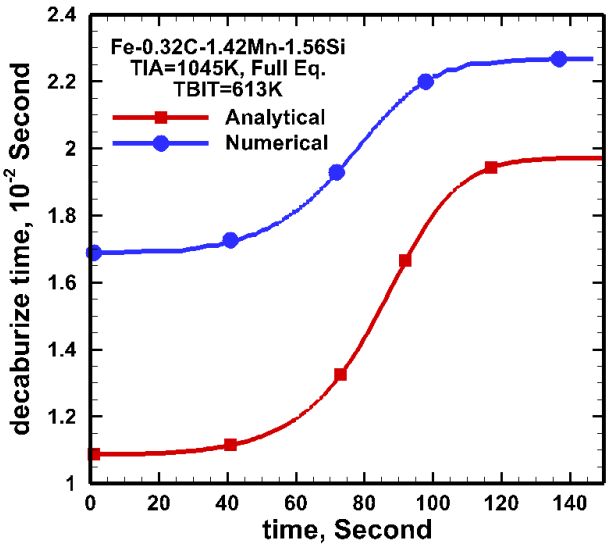

Figure 5.4: The decaburize time using analytical and numerical methods

The target of this model is to figure out the upper bound of the austenite stability after BIT. In other words, the maximum carbon content is required form this model

which can be approached by the numerical solutions.

5.3 Calibration of Model Parameters

There are several parameters necessary for calculations. From experiments, the grain size of the austenite is about 10 μm which is the only parameter obtained from experiments in this work. In order to realize how the other variables affect the results from this model, a series of test is made.

According to the work done by Jacques and his co-workers, N_0 and β_a are the two fitting parameters for this model [34]. These two parameters are reported as $N_0 = 2 \times 10^{-4}$ and $\beta_a = 1.5$.

In Fig. 5.5, seven sets of these two parameters are included in the calculations. Comparing the cases with different N_0, the incubation time is obviously postponed with smaller N_0. This matches the definition of N_0: the number of potential nucleation sites.

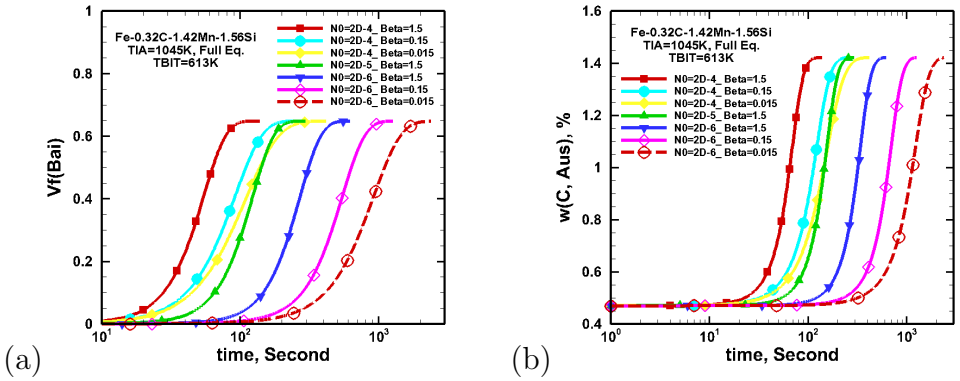

Figure 5.5: The CCT diagram calculated by different parameters for BIT at 613 K, (a) $Vf(Bai)$ (b) w^{γ}_{C2} as functions of time

Another interesting comparison is β_a which is the fitting parameter that adjusts

the rate of auto-catalytic nucleation in Eq. 5.5.

In calculations while $N_0 = 2 \times 10^{-4}$, the change of the β_a does not make obvious difference; however, while $N_0 = 2 \times 10^{-6}$, β_a clearly tilts the transformation curve. This is because the transformation rate is dominated by larger N_0 for the first three curves. On the other hand, if the primary nucleation is not rapid, the larger β_a results in higher auto-catalytic nucleation rate and the transformations finishes in shorter times.

From these two figures, it can be seen how important these two parameters are for the determination of the transformation time. Unfortunately, in different experimental environments or for different alloys, the new fitting value is required in order to predict more accurate heat treated time. However, our calculations suggest that the transformations stop with the same bainitic ferrite volume and w_{C2}^{γ}, regardless of the actual rate of transformation. This can be attributed to the fact that we consider that carbon diffusion is strictly confined by the bainitic ferrite plate. Whenever the average carbon content of unchanged austenite reaches $w_C^{T_0'}$ the transformation stops no matter how long it takes for the alloy to reach this point. Therefore, the carbon concentration in austenite film is not related at all to the transformation rate. It is thus necessary to emphasize the fact that instead of predicting accurate heat treated time, it is more focused on estimating the upper bound of w_{C2}^{γ}. Since neither N_0 nor β_a can cease the transformation, they are chosen the same values as Jacques' work [34].

Another shape of bainitic ferrite plate was proposed in 2004 [67]. The bainite sub-unit is assumed as in rectangular shape and the aspect ratio is 0.02. The volume of it can be presented as: (m^3)

$$V_{UB,Rec.} = 2.0 \times 10^{-17} \times (\frac{T - 528}{150})^3 \tag{5.10}$$

The calculations in Fig. 5.6 is essentially applying the kinetic model for estimating w_{C2}^{γ} in the end of the BIT at different temperature. Even the Eq. (5.4) and (5.10) recommend different volumes for bainite sub-unit, the calculated w_{C2}^{γ} are the same under the same T_{BIT}. It is worth to note that the bainite sub-unit is pretty small in volume comparing to austenite. The observed austenite grain volume is about 10^{-15} m^3 and the bainite sub-unit is predicted as 10^{-17} m^3. Therefore, the small change of the bainite sub-unite volume does not cause significant changes of the results.

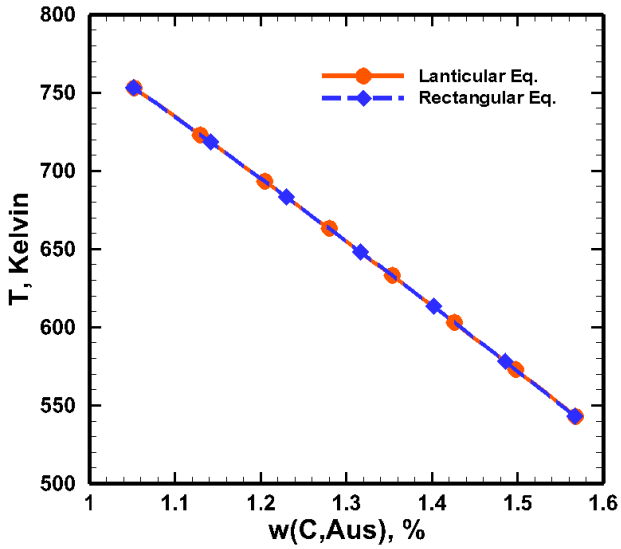

Figure 5.6: The comparison between different approaches to the volume of bainite sub-unit

Fig. 5.7 is the phase diagram with the w_{C2}^{γ} calculated by kinetic model. There are two different calculations in this diagram: one is calculated after 1045 K equilibrium calculation and the other is based on empirical data and reverse calculation as Table 4.2. Measuring from experiments, w_{Mn}^{γ} is 0.28% lower than equilibrium value which

makes 6 K higher in TMS (by Eq. (3.4)). Therefore, the calculations with empirical inputs is higher than the equilibrium one with the same carbon content, even through the difference is small. The other observation is the comparison of the upper limit. With only 0.06% carbon difference after IA, the difference of w_{C2}^{γ} is as high as 0.15% as Fig. 5.7(a).

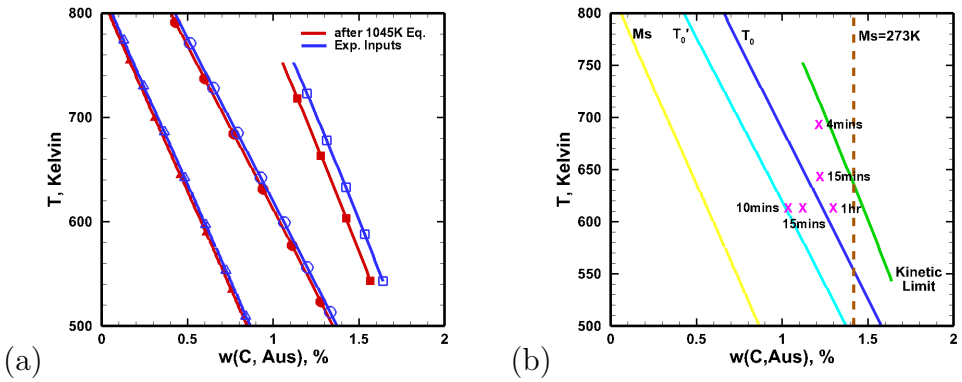

Figure 5.7: The phase diagram for BIT treatment (a) the calculations by different inputs (b) comparing to the experiments [97, 62]

Comparing the experimental results with the calculation based on experimental data as Fig. 5.7(b), w_{C2}^{γ} is obviously higher than T_0'. In some cases, the carbon content is close to T_0 and this is the reason why T_0 is recommended as the design guide. However, all the cases present higher w_{C2}^{γ} than T_0 in the end of the heat treatment. It is clear that the kinetic model provides the upper bound of the bainitic transformation. Most importantly, the optimum heat treatment window (as Fig. 4.4) exists while T_{BIT} is in the range between 590 K to 625 K. The martensitic transformation can be avoided in this window.

Fig. 5.8 is the comparison with experimental results.

There are two calculations utilizing kinetic model with the initial carbon contents (w_{C1}^{γ}) 0.53 and 0.63 wt%. By the kinetic model, the predicted volume fraction of austenite is about 10% more than T_0. Comparing to the experiments, the results by kinetic simulation stand the highest state of retained austenite. Another interesting point is that while T_{BIT} is higher than 663 and 693 K, the martensitic transformation occurs in the final cooling.

This causes a decrease of the austenite volume fraction at higher T_{BIT}.

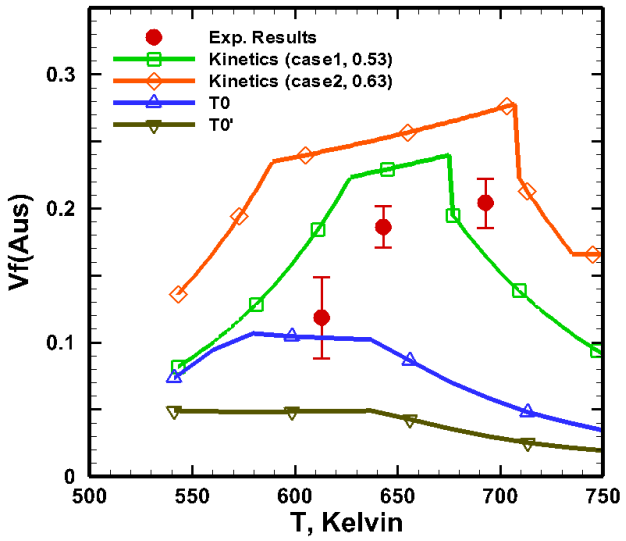

Figure 5.8: The volume fraction of retained austenite [62]

Comparing to the experimental results, this modified kinetic model provides one of the extreme cases of the carbon distribution which stands the maximum C-enrichment in retained austenite. The cause for the non-homogeneous carbon distribution is the time and space intervals of the successive bainitic nucleations under the displacive transformation assumption.

At high T_{BIT}, the size of the bainite sub-unit is large ($\sim (\frac{T-528}{150})^3$). According to displacive transformation model, the growing process of the bainitic ferrite is similar to martensitic transformation which grows to 10nm in time scale of 100ps [74]. The growing rate ($10^{-6}\ m^2/s$) is in several orders higher than the carbon diffusion in austenite ($10^{-21}\ m^2/s$, as Fig. 5.9). Even the driving force for bainitic transformation is relatively small, the phase transition rate is higher and the space between bainite plate is small and the carbon enrichment in retained austenite is more close to the extreme case predicted by kinetics at high T_{BIT}. On the other hand, if T_{BIT} is very low, the size of the bainite sub-unit is relatively small which allows carbon diffusing in larger residual austenite. This explains why at low temperature, the formation of nano-bainite terminates at compositions consistent with the T_0' limit.

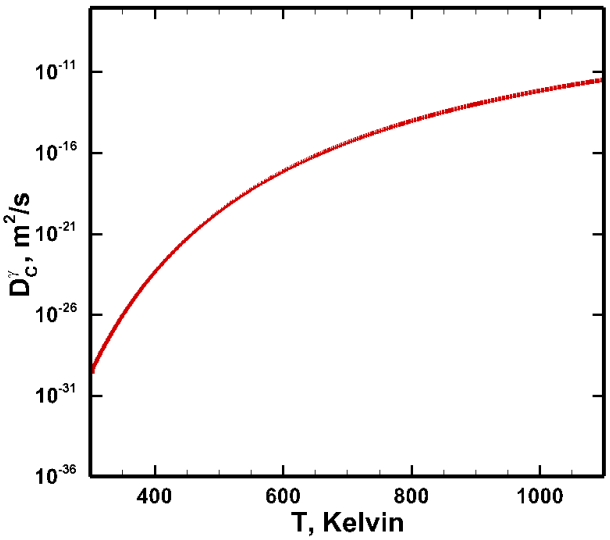

Figure 5.9: The diffusivity of carbon in austenite

To conclude the theoretical analyses, the carbon enrichment in retained austenite

is the result of the competition between carbon diffusion and phase transition. At high T_{BIT}, w_{C2}^{γ} is more close to the maximum value which can be estimated by kinetic model proposed in this work; at low T_{BIT}, w_{C2}^{γ} is more close to $w_{C2}^{T_0'}$. At middle T_{BIT}, T_0 can be utilized to predict the w_{C2}^{γ} after BIT treatment.

6. FINDING AN OPTIMUM HEAT TREATMENT SCHEDULE FOR TRIP-ASSISTED STEELS

6.1 Alloy Design

Optimization essentially consists of the determination of a set of values for the degrees of freedom that determine the response of a system that maximize/minimize such response. In the particular case of the optimization of materials response, one must manipulate all factors that contribute to the material performance. These factors include not only the chemical constituents of the material, but also the processing routes necessary to obtain the desired microstructure. When one considers the fact that most materials actually consist of many components and have to undergo very complex processing routes, the optimization problem seems to be rather hard. One can consider for example the case of steel alloys, which are perhaps some of the most complex materials system of practical use. In the case of stainless steels, for example, thirteen elements are considered in design process [89]. If the heat treatment is included, at least 15 variables must be taken into account. In an optimization framework, the search for the optimal set of composition/heat treatment parameters represents the search over a 15-dimensional space. It is therefore not unexpected that, after centuries of investigation, steels are still being optimized. In this section, we will discuss the process used to optimize the conventional two-stage heat treatment to control the phase constitution in TRIP-assisted steels.

To improve the mechanical performance of the TRIP steel, the design process can be simply divided into three distinct steps: material selection, microstructure design, and performance testing (as shown in Fig. (6.1)). In this work, once the material is selected, the CALPHAD method is utilized in conjunction with kinetic

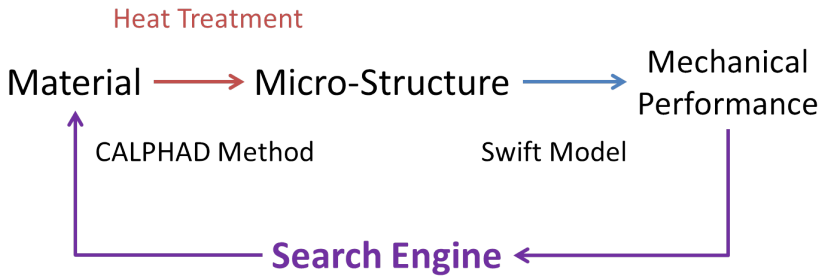

Figure 6.1: The alloy designing process in this work

models to predict the phase constitution after different heat treatment schedules, as demonstrated in the previous chapters.

6.2 Predicting Mechanical Performance

In order to link the predicted phase constitution to the mechanical performance of the microstructure, the Swift model (Eq. 6.6) is used to predict the stress-strain characteristics of multi-phase microstructures [86, 56, 28]. The model can be simply described using the following equation:

$$\sigma_i = K_i(1 + \varepsilon_{(0,i)}\varepsilon)^{n_i} \tag{6.1}$$

where i stands for the phase; (i. e. ferrite, bainitic ferrite, austenite and martensite). K_i, $\varepsilon_{(0,i)}$, and n_i are the phase parameters for yield stress, slope and curvature of the stress-strain curve. Under iso-strain condition, the stress of the alloy can be represented as function of the collective effect of the phase constituents:

$$\sigma = \sum \sigma_i V f_i \tag{6.2}$$

The parameters for the model are based on empirical results for the alloy with

nominal compositions: Fe-0.29C-1.42Mn-1.41Si and are listed in Table 6.1 [56, 45]. It is understood that the mechanical properties of the alloy depend on not only the phase constituent but also the chemical composition, w_C^γ especially [68, 1], as well as the grain size, dislocation density, temperature and strain rate etc. Although the latter parameters are not explicitly considered in the model, some of the different factors are implicitly considered through the factor K_i. In this work, the stress is estimated by linear extrapolation of the predictions using these two parameter sets:

$$\sigma = \sigma_A + (\sigma_B - \sigma_A)\frac{w_C^\gamma - 1.25}{0.25} \tag{6.3}$$

Table 6.1: The parameters used in Swift-type equation; model A: w_C^γ=1.25 wt%; B: w_C^γ=1.5 wt%; BCC phase stands the ferrite and bainitic ferrite [56, 45]

	Phase	K_i, MPa	$\varepsilon_{(0,i)}$	n_i
A	Austenite	720	62	0.3
A	BCC	475	55	0.27
A	Martensite	2000	800	0.005
B	Austenite	1130	80	0.2
B	BCC	720	50	0.175
B	Martensite	2000	800	0.005

With the prediction of the stress-strain curve, the necking can be predicted by the following condition[41]:

$$\frac{d\sigma}{d\varepsilon} = \sigma \tag{6.4}$$

To test the theoretical model, several experiments with different heat treatment schedules are performed (by Ruixian Zhu) in the alloy of nominal composition Fe-0.32C-1.42Mn-1.56Si [97]. The details of the experiments are listed in Table 6.2. The IA treatments consists of heating 1045, 1053, or 1083 K for two hours. Three T_{BIT}s,

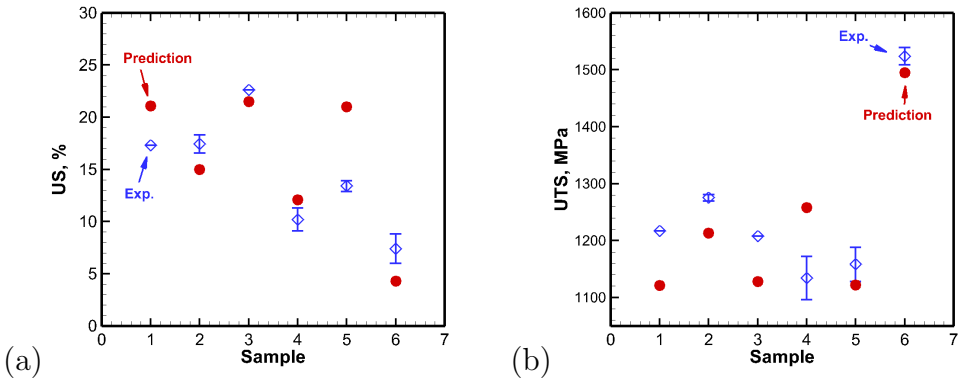

Figure 6.2: The predicted mechanical properties comparing to the experimental results [97]

613, 643, and 693 K, are selected for three different time spans. According to the physical models, the resulting microstructures after different $T_{IA}-T_{BIT}$ combinations are predicted taking into account the partitionless nature of the bainitic transformation (T_0 thermodynamic limit), as well as the prediction of athermal martensite fraction according to the temperature of quenching relative to the M_S temperature of the alloy at a given composition. The mechanical properties of the resulting microstructure are estimated using Eq. 6.3. The results are included in Fig. 6.2. While there are obvious discrepancies between experiments and predictions, the theoretical modelling provides results that are in qualitative agreement with experiments. This is remarkable when one considers that the only input to the models were the two treatment temperatures. More importantly, the results suggest that the different heat treatment schedules result in similar rank ordering when comparing the actual experimental results and the predictions.

While in the discussion above we focused on the effects of heat treatment schedule on mechanical performance, when optimizing the performance of TRIP steels, one must consider at least five degrees of freedom (input variables), including chemical

Table 6.2: The heat treated temperatures (Kelvin) and time for BIT treatment in experiments; all the IAs are treated for 2 hours

Sample	T_{IA}	T_{BIT}	BIT time
1	1045	693	4
2	1045	613	60
3	1045	643	45
4	1053	613	60
5	1053	693	4
6	1083	613	60

compositions (w_C, w_{Mn} and w_{Si}) and two heat treatment temperatures (T_{IA} and T_{BIT}). Of course, one could in principle approach this problem experimentally, at great cost. Alternatively, one could take the predictive models developed in this work and proceed with a systematic search for optimal combinations of composition and heat treatment schedules. When one considers the high dimensionality of this problem, it is evident that a more efficient strategy must be used in order to find optimal solutions. In this work, we address this optimization problem through the use of Genetic Algorithms.

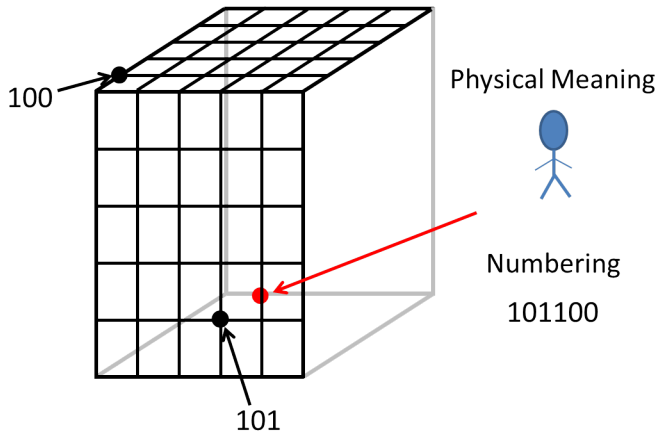

Figure 6.3: The schematic diagram of the domain searching by genetic algorithm.

6.3 Genetic Algorithm-based Alloy Design

Genetic algorithm (GA) is a computer-based optimization scheme that mimics natural selection in the sense that the population of possible optimal solution of the problems is subject to random variation, subject to non-random selection, that is: survival of the fittest [36]. In order to implement GA optimization, the search domain, which corresponds to the phenotype domain, is discretized, as illustrated in Fig. 6.3. The refinement of the discretization is limited by the capacity of the computer memory to be used. For example, if 4 bits of memory is utilized for one variable, the domain is evenly divided into 16 (2^4) segments and each segment is then represented through binary encoding, which in turn can be considered to be the genotype domain.

It is shown in Fig. 6.4 that most of the GA operators are working in genotype domain because of the numerical convenience of binary systems.The first generation with a certain amount of strings in genotype domain is randomly selected as the initial seeds. Based on these strings, the decision maker assigns the fitness according to the physical properties stored in phenotype strings. This evaluating process is similar to the calculations in the previous chapters, for example the prediction of the microstructure of the TRIP steel. By these fitness, most of the individuals with poor performance are eliminated and the best two are remain and marked in the genotype table. In order to keep the size of the group constant, the outstanding individuals have been reproduced to fulfill the openings left by the individuals eliminated from the population. Subsequently, the cross-over and mutation are applied to create the diversity in the population. First, the strings are randomly paired. Between two strings, a probability is assigned (50% in this work) for exchanging the chromosome(s). After the cross-over, each new string is examined by a mutation

rate, in this work, this rate is defined as

$$P = \frac{C}{x \cdot A} \tag{6.5}$$

where C is the number of chromosome (size of memory) of each string; x is the number of variables of one string and A is the number of strings in one generation.

During this process, a certain amount of chromosome is mutated. Take Fig. 6.4 for example, there are six chromosomes keeping two variables in each string, and the population of the generation is seven. Therefore, the recommended mutation rate is $6/(2 \times 7) \cong 0.43$. After hundreds of thousands evolutions, the highest fitness is improved and the group is moving toward the high fitness direction.

6.4 Preliminary Evaluation of GA-based Optimization

A test calculation is applied to maximize the volume fraction of retained austenite. Because only two variables are involved, the total calculated generation is 500 and each one contains 6 strings. As Fig. 6.5 shows, the first generation is randomly selected from X_1 and X_2. According to Table 6.3, the two temperatures, T_{IA} and T_{BIT} are the inputs in decision maker which is predicting the volume fraction of retained austenite. To maximize the volume fraction of retained austenite, the higher fitness is assigned for higher Vf(aus) alloy while (1) Vf(Aus) $\geq$ 20%, the fitness is 0.0051; (2) Vf(Aus) is between 15 to 20 %, the fitness is 0.0041; (3) Vf(Aus) is between 10-15 %, fitness is 0.0031; (4) Vf(Aus) is less than 10 %, fitness is 0.0021; (5) others, fitness is 0.0000101. Before 500 generations are calculated, the survived two strings are the seeds for GA operators. If the population is not converged, the calculation continues; on the other hand, if the difference in the genetic variance of the chromosome is lower than 5%, the calculation is converged and the calculation will be restarted to examine possible trapping around local minima.

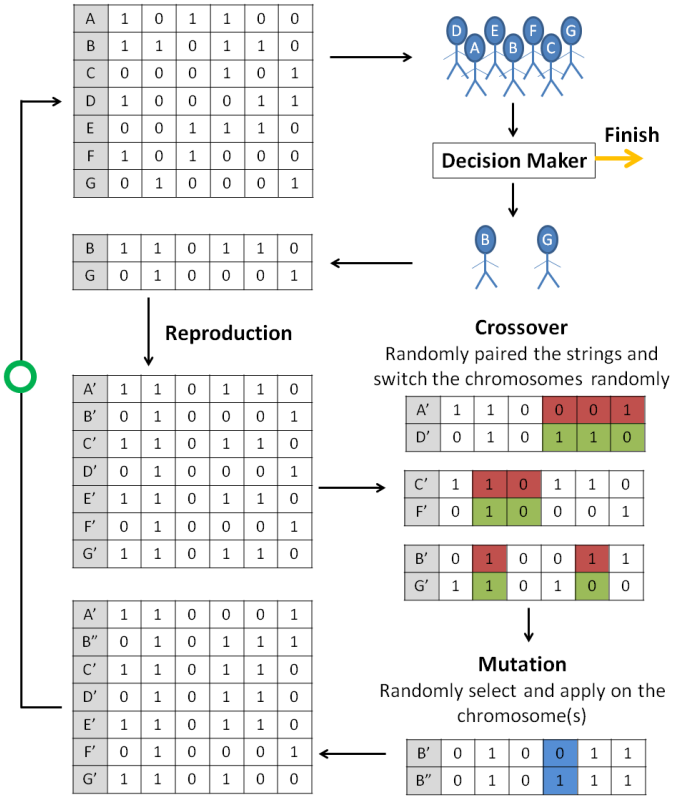

Figure 6.4: The schematic diagram of the genetic algorithm

According to the initial setting, the maximum number of calculations is 3000; but, the effective calculations are 2871 because of some multi-selected conditions and some failed calculations. The failed calculations include (1) T_{IA} is not higher than Ac_θ at which cementite remains, (2) the volume fraction of austenite is less than 10% after IA or (3) T_{BIT} is higher than bainite start temperature T_{Bs}. These invalid calculations are assigned the lowest fitness by the decision maker.

Fig. 6.6 shows an schematic diagram of calculation process with T_0 limitation using GA. Before the calculation, these two dimensionless domain are discretized. Initially, the population of the first generation is randomly generated which contains of four strings (as the black points) in this example. According to the decision maker,

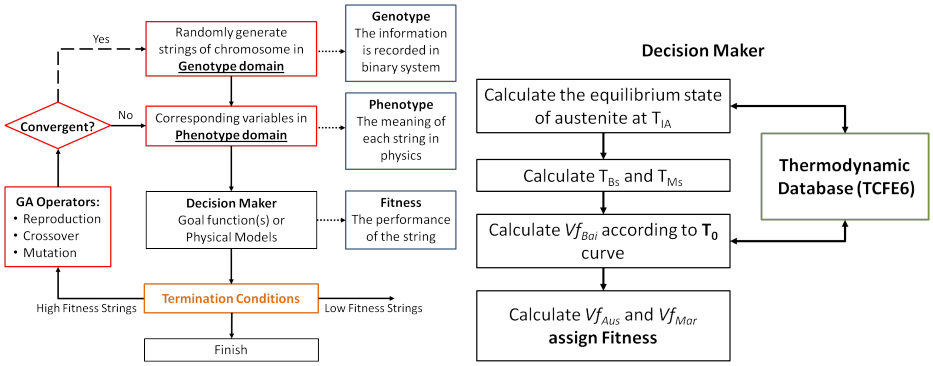

Figure 6.5: The flow chart for optimization calculation

the filled points are the two with highest fitness; therefore, these two are kept for the next step. In Fig. 6.6(b), the next generation is produced and manipulated (the crossover and mutation) based on the information of the survived two. If the similarity of the chromosome is too high, the calculation is defined as converged and the population will be re-initiated. The ideal evolution is specified as Fig. 6.6(c): the average fitness of the population is increasing with the number of the evolution. Repeating the process, Fig. 6.6(d) is generated after 10 generations. It can be seen that either highest or average fitness is improving after generations by the leading of the fitness value.

In order to examine the effects of the 5% converging setting, another calculation is proceeded with 1% similarity among the strings. The effective number of calculations with CC=1% is 2802 which is less than the one with 5% condition. In Fig. 6.7 (a) and (b), x axis is the number of the generation and y axis is the average fitting value of the generation. It can be understood that with more strict converging condition, the calculations more focus on one area; on the other hand, if the acceptable difference is large, the calculation will be restarted more frequently. This is the reason why more points are calculated with 5% conditions (as Fig. 6.7 (c)(d)). Once the calculation

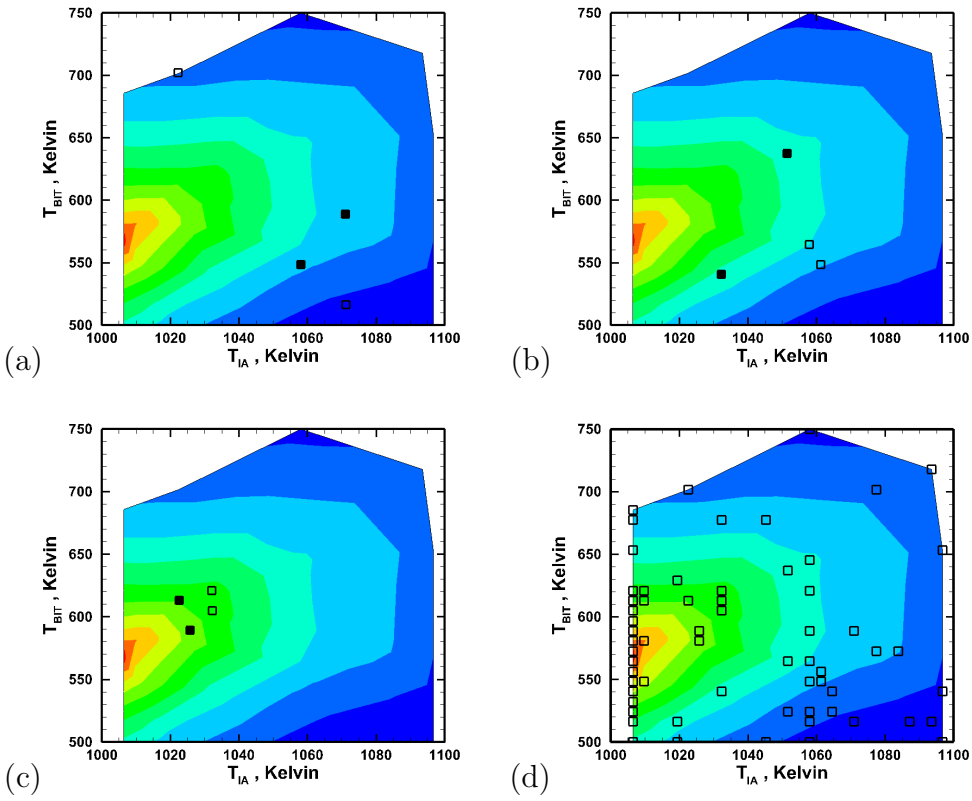

Figure 6.6: The schematic process of GA

is restarted, the randomly selected strings may explore more area in the searching domain which helps to understand the effects of the heat treatments. However, if the optimization involves more variables or larger computer memory, more strict condition is required in order to increase the accuracy.

6.5 Maximizing Retained Austenite of Fe-0.32C-1.42Mn-1.56Si Alloy

In this section, the optimum heat treated temperatures for Fe-0.32C-1.42Mn-1.56Si alloy are examined by GA organized calculation. According to the physical models, the calculated T_{IA} is limited in the range of 1000 to 1100 K and 529 to 900 K for T_{BIT}. 5 bits computer memory is utilized for each temperature, therefore,

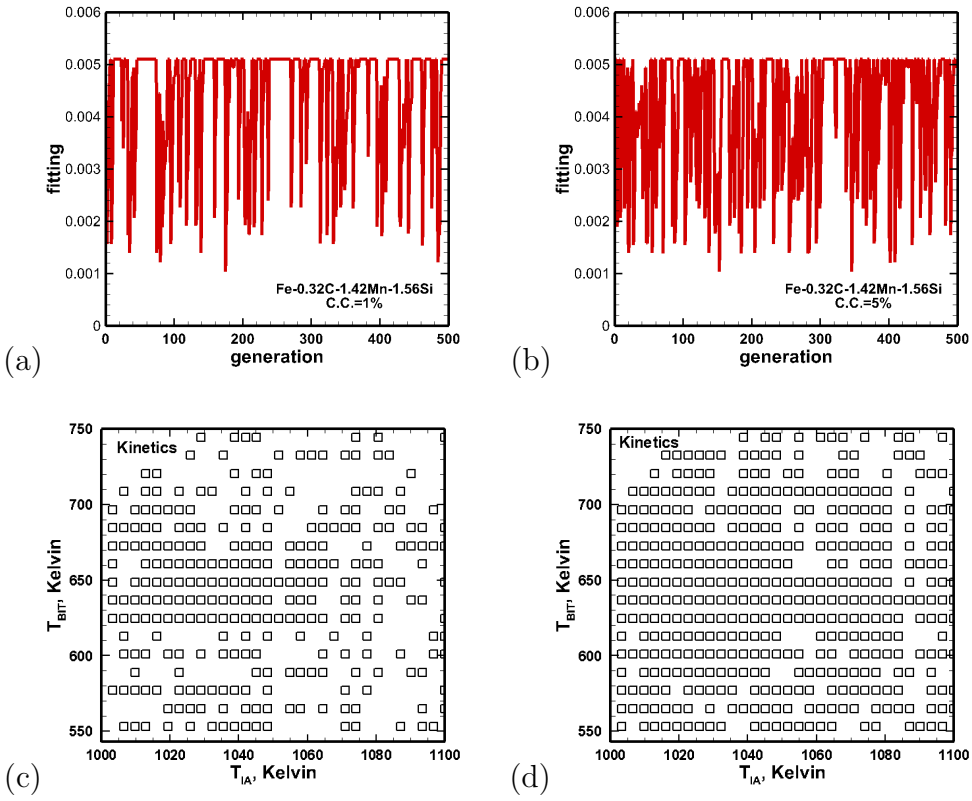

Figure 6.7: The compare between different converging conditions (C.C.) (a)(c) 1% (b)(d) 5%

there are 32x32 (1024) potential temperature sets for calculations (as Table 6.3).

Fig. 6.8 represents the results by optimizing calculations in which the T_0', T_0 and kinetic model are considered for BIT. As discussed in previous chapters, as long as the heat treatment time is sufficient, T_0' stands the lower bound and kinetic model provides the upper bound of the bainitic transformation. As a consequence, for Fe-0.32C-1.42Mn-1.56Si alloy, the lower bound of the maximum volume fraction of austenite is 11.6% which can be achieved by 1003 K T_{IA} and 529 K T_{BIT}. The upper bound of maximum austenite of this alloy by the kinetic model is 23.5% in volume after 1016 K IA and 685 K BIT heat treatment. After this process, there

Table 6.3: The possible variables for GA calculation (Kelvin); the string in genotype domain consists of X_1 and X_2; T_{IA} and T_{BIT} are the corresponding temperatures in phenotype domain

X_1	1	2	3	4	...	31	32
T_{IA}	1000	1003.125	1006.250	1009.375	...	1096.875	1100
X_2	1	2	3	4	...	31	32
T_{BIT}	529	540.594	552.188	563.781	...	888.406	900

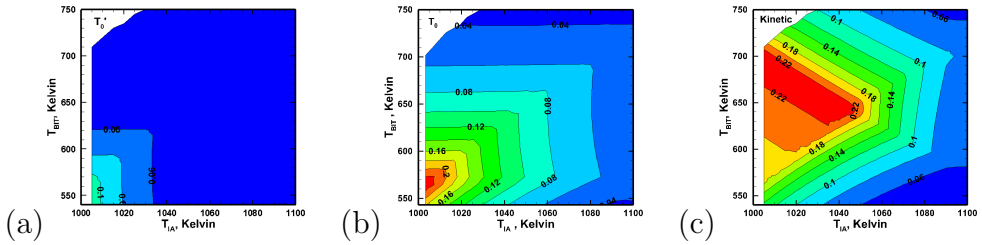

Figure 6.8: The predicted volume fraction of retained austenite while bainitic transformation stops by (a) T_0' (b) T_0 (c) kinetic model

are about 1% martensite, 30% bainitic ferrite in the final microstructure and the rest is ferrite. It is more clear in Fig. 6.9, if carbides are totally suppressed, the martensitic transformation can be avoided during the heat treatment while T_{BIT} is between 590 to 685 K. The stability of the retained austenite can be controlled by T_{BIT} in this temperature range; as T_{BIT} is closer to 590 K, more bainite is formed and the retained austenite is more stable.

Comparing the different criteria to terminate the bainitic transformation during BIT in Fig. 6.8, the profile of the contours of the austenite volume fraction are very different. At lower T_{BIT}, the martensitic transformation take place after IA treatment. But, because of the negative slopes of the curves, the carbon content is higher than the other cases at higher T_{BIT}. In Fig. 6.9, it can be seen that the martensitic transformation can not be suppressed in T_0' limitation. While more

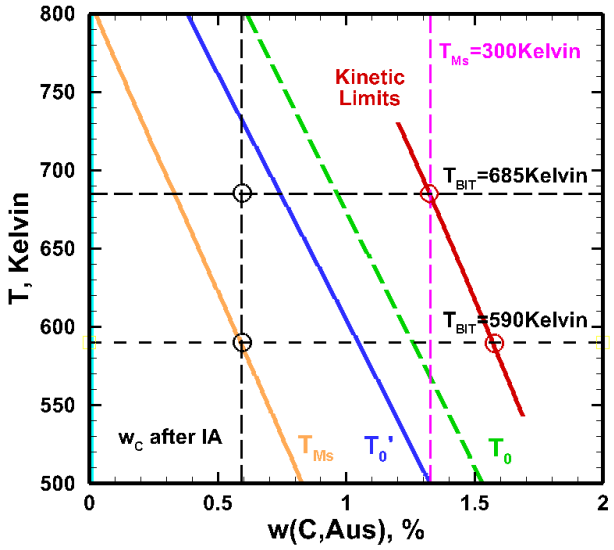

Figure 6.9: The phase diagram of Fe-0.32C-1.42Mn-1.56Si after T_{IA}=1016K

ferrite is retained at lower T_{IA}, austenite is more stable after IA and T_{BIT} can be even lower to form more bainitic ferrite. Therefore, lower T_{IA} and T_{BIT} are preferred in T_0' calculation. On the other hand, in T_0 prediction, the similar phenomenon can be observed to select lower T_{IA}, but the optimum T_{BIT} is the cross point of T_0 and T_{Ms} = 300 Kelvin which is about 580 Kelvin. As for kinetic model, as long as T_{BIT} is lower than 685 K, it is possible to suppress the martensitic transformation with properly selected T_{IA}. However, more bainitic ferrite is allowed to form which consumes austenite at lower T_{BIT}. So, the optimum heat treatment for maximizing austenite is with T_{IA} being lower than 1050 K and T_{BIT} higher than 630 K.

6.6 The Optimum Heat Treatment Temperatures for Fe-0.32C-1.42Mn-1.56Si TRIP Steel

Except for martensite, cementite which is the carbon sink during the heat treatment is another undesired phase in TRIP steel. The more cementite is present in

the microstructure, the lower the stability of austenite. In order to avoid cementite formation, one can control the treatment temperature and time. From the thermodynamics point of view, as T_{IA} is higher than Ac_θ and para-equilibrium $\gamma - \theta$ is avoided, cementite can be suppressed. Four more situations are assumed: (1) equilibrium IA with T_0 (2) para-equilibrium IA with T_0 (3) equilibrium IA with T_0 and para-equilibrium $\gamma - \theta$ (4) para-equilibrium IA with T_0 and para-equilibrium $\gamma - \theta$. In case (3) and (4), the maximum carbon enrichment of retained austenite is the minimum value of T_0 and para-equilibrium $\gamma - \theta$.

In these four cases, the Eq. 6.3 is utilized to estimate the mechanical properties, uniform strain (US) and ultimate tensile stress (UTS). In addition to the maximization of either US or UTS, another fitness is proposed for optimizing the mechanical performance. The ideal microstructure is the one (1) with maximum volume fraction of retained austenite (2) minimum carbon content in austenite while maintaining its stability against martensitic transformation and (3) less martensite. With these assumptions, the fitness is defined as:

$$fitness = \frac{Vf(Aus)}{0.01 w_C^\gamma (0.001 + Vf(Mar))} \tag{6.6}$$

Therefore, there are three optimizations for (a) US (b) UTS and (c) fitness in each case. Each optimization includes 10 individuals and 2000 generations. In all of the calculations, the Vf(aus) must be higher than 5%, otherwise the result is not counted in this work.

Fig. 6.10 includes the results in case 1. The effective number of the calculations is 728. As Fig. 6.10(a), the predicted US and UTS are listed as function of fitness. In this case, the highest fitness indicates the heat treatment with the highest US. The highest predicted US is 23.4% after 1003 Kelvin IA and 566 Kelvin BIT treatment.

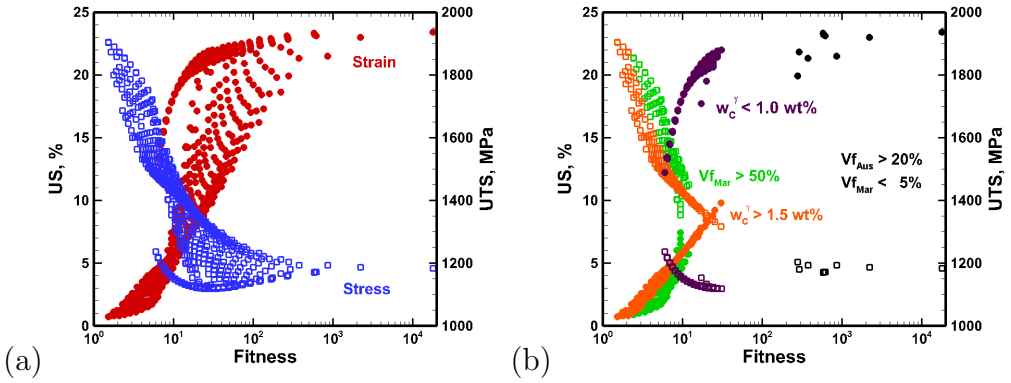

Figure 6.10: The predicted mechanical properties with fitness

The ideal microstructure contains 23.5% retained austenite, 52.9% ferrite and 23.6% bainitic ferrite. No martensite would be observed under this condition. The route of the heat treatment is illustrated in phase diagram as Fig. 6.13(a).

The further analysis can be found in Fig. 6.10(b). In order to achieve w_C^γ higher than 1.5 wt%, T_{BIT} must be low. More martensite is forming after the quenching from T_{IA}. On the other hand, if w_C^γ is lower than 1.0 wt%, martensitic transformation can be observed after BIT treatment. Even the stability of the retained austenite is low, the alloy is not achieving it's best mechanical performance. From this analysis, it can be seen that the ideal w_C^γ should be between 1.0 to 1.5 wt% to maximize the retained austenite and minimize the volume fraction of martensite. Treating in this way, the US of this alloy is maximized.

Following the previous analyses, the toughness is predicted under three different conditions using Eq. 6.4 ans resulted as Fig. 6.11. Because of 5% Vf(Aus) criterion, the area of the T_0' contour is relatively smaller than the other two. The profiles of these plots match the ones for Vf(Aus) contours. Without first carbon enrichment from ferrite at high T_{IA}, austenite is not stable enough for lower T_{BIT}. The volume

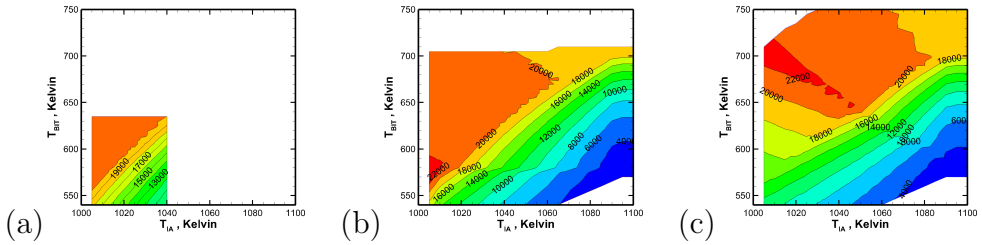

Figure 6.11: The predicted toughness after different heat treatments based on (a) T_0' (b) T_0 (c) kinetics

fraction of retained austenite does not mean everything comparing to Fig 6.8. From these three figures, it can be seen that low T_{IA} provides the bigger window for optimal T_{BIT} in this case. Fig. 6.12 consists of the high toughness area in these three cases. Considering the upper and lower bounds of the microstructures, the optimum treatment for high toughness can be obtained with T_{IA} being lower than 1045 K and with T_{BIT} between 630 to 650 K.

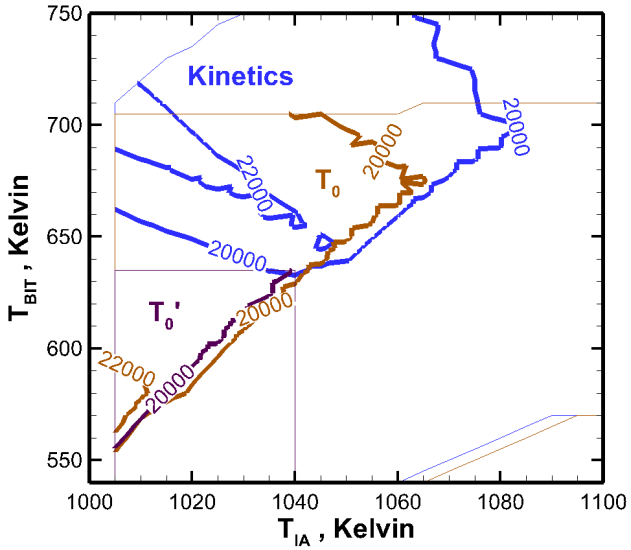

Figure 6.12: The predicted toughness after different heat treatments

The optimum conditions for maximizing fitness for the other three cases are illustrated in the phase diagrams in Fig. 6.13. For case 1 and 2, the optimum T_{IA}s are just above Acθ and T_{BIT}s are the cross points of T_0 and $T_{Ms} = 300$ Kelvin. As case 3 and 4, the optimum T_{BIT}s are the cross points of T_0 and para-equilibrium $\gamma - \theta$. For IA, the window is very different from the other two cases. As shown in Fig. 6.13(c) and (d), a window of T_{IA} can be applied with the same T_{BIT} for the same mechanical property. It is because the model in Eq. 6.6 does not consider the difference between ferrite and bainitic ferrite. The contributions to the mechanical properties from these two phases are the same. Therefore, within the T_{IA} window, the sum of the Vf(Fer) and Vf(Bai) is not changed.

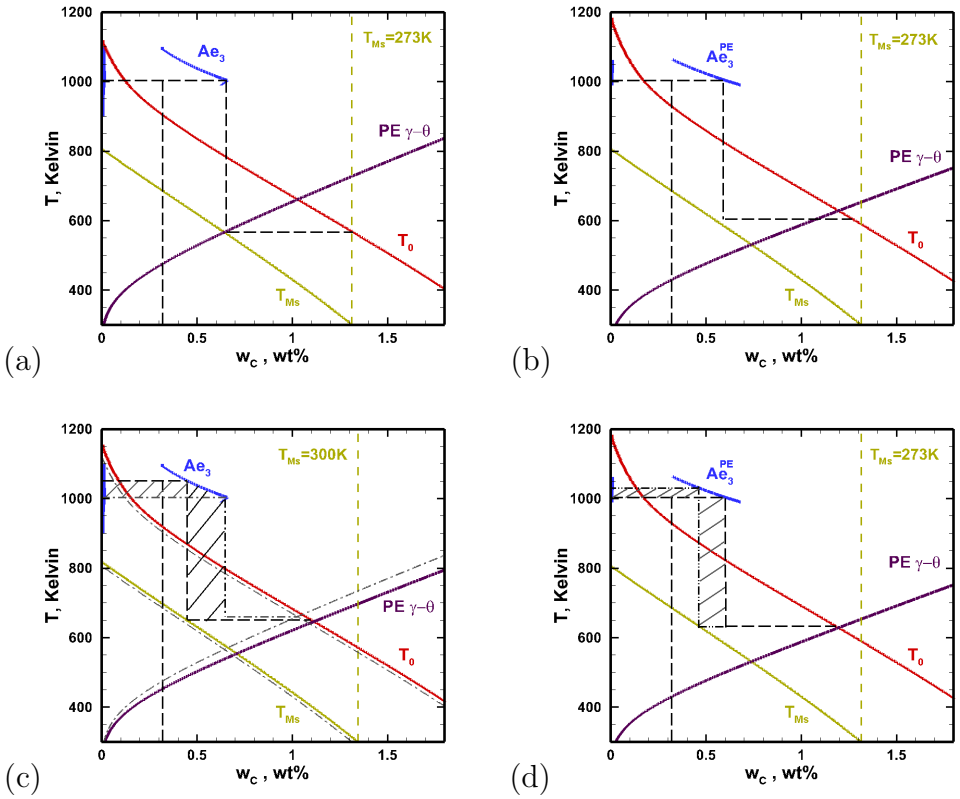

Figure 6.13: Phase diagrams for different heat treatments (a)-(d) for cases (1)-(4)

The predicted mechanical performance is listed in Table 6.4. It can be seen that while the alloy is more close to equilibrium (case 1 and 3), the ductility is better than the short IA treatment (case 2 and 4). The other important factor is the para-equilibrium $\gamma - \theta$. Comparing case 1 to 3, to suppress the formation of cementite according to para-equilibrium condition will sacrifice about 1.5 % strain if the incubation time of cementite is long enough. For this specific alloy, the optimum heat treatment for maximizing the fitness is that (1) T_{IA} is higher than Acθ (2) long IA treatment (3) selecting the cross point of T_0 and para-eq. $\gamma - \theta$ as T_{BIT}.

Table 6.4: The predicted mechanical properties of the four cases

case	1	2	3	4
T_{IA} (K)	1003	1003	1003-1050	1003-1006
T_{BIT} (K)	566	604	651-660	632
Vf(Aus)	0.23	0.16	0.09	0.11
Vf(Bai)	0.24	0.28	0.17-0.41	0.27
Vf(Fer)	0.53	0.47	0.30-0.53	0.47
Vf(Mar)	0.00	0.09	balance	balance
w_C^γ	1.32	1.27	1.10	1.18
US, %	23.4	21.0	22.0	20.8
UTS, MPa	1183	1159	1120	1137

7. OPTIMIZATION OF CHEMICAL COMPOSITION IN TRIP STEEL

To improve the mechanical performance of the TRIP steel, a properly selected chemical composition within a reasonable domain is required. As the analyses in the previous chapters show, the domains for six elements are listed in Table 7.1. With the variation of chemical composition, the optimization of the heat treated temperatures are also required. Fe-0.1C binary phase diagram is one of the extreme cases (as Fig. 7.1). According to this diagram, the highest temperature at which ferrite can exist (Ac_3) is 1142 Kelvin which is chosen as the upper temperature boundary of T_{IA} for GA. On the other hand, T_0' is about 934K which is also set as the lower boundary of the T_{IA}. If the alloy contains maximum alloying of austenite stabilizer and minimum Al (Fe-0Al-0.5C-0.03Cu-2.5Mn-2Ni-1.5Si), T_{MS} is about 558 K which is predicted by Eq. 3.4. According to Eq. (4.4), 90% Austenite transforms into Martensite at 350 K, therefore, this temperature is picked as the lower boundary of T_{BIT}. These conditions are listed in Table 7.1.

Table 7.1: The searching domains of chemical composition and heat treated temperatures for GA calculation (-wt%)

	min.	max.		min.	max.		min.	max.
w_C	0.10	0.50	w_{Mn}	0.50	2.50	w_{Si}	0.50	1.50
w_{Al}	0.00	2.00	w_{Cr}	0.00	1.33	w_{Ni}	0.00	2.00
T_{IA}	934	1142	T_{BIT}	350	934			

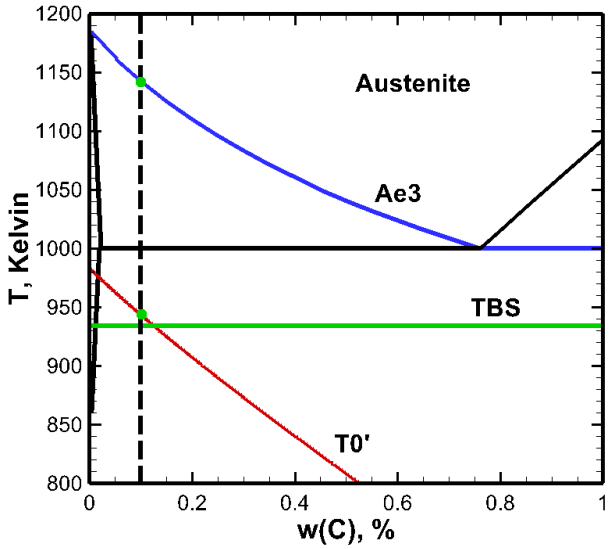

Figure 7.1: The phase diagram of Fe-0.1C (wt%)

7.1 Fe-C-Mn-Si TRIP Steel

7.1.1 T_0 Limitation

According to the discussion in the previous chapters, the level of the C-enrichment in retained austenite can be predicted using either thermodynamic or kinetic model. At intermediate T_{BIT}, T_0 is a better predictor of the carbon enrichment at short bainitic transformation time. In this section, it is assumed that (1) the alloy is at equilibrium state after IA treatment (2) the carbon enrichment achieves the minimum value of T_0 and para-equilibrium $\gamma - \theta$. The optimization is based on μ-GA to search the domain as 7.1 in Fe-C-Mn-Si alloy with the calculations of 10 individuals, 5,000 generations. It is the same as the previous chapter: three optimizing targets (1) maximizing fitness (2) maximizing US (3) maximizing UTS are included to search each direction as deep as possible.

Even though the microstructures are the same, the fitness may be different. Fig.

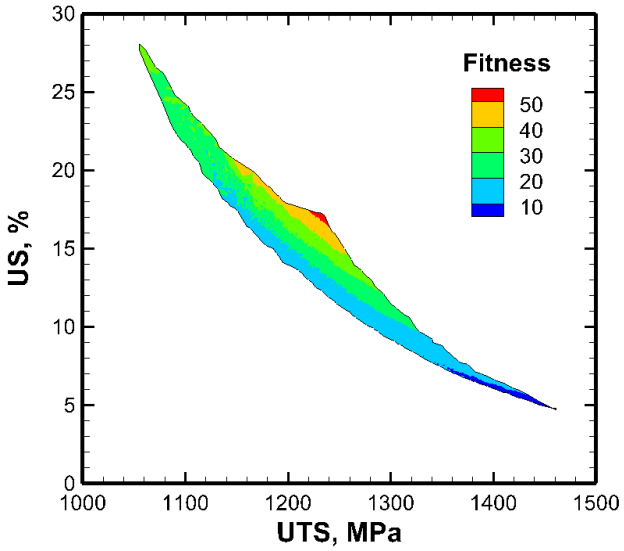

Figure 7.2: The predicted fitness of the alloy with different mechanical properties

7.2 includes 3636 highest fitness with the same US-UTS samples of all the samples. It can be seen that the high elongation sample is with higher fitness than the lower strain one. There are two mechanisms contribute to the high elongation alloys (1) high volume fraction of ferrite and (2) low carbon content in retained austenite. It is more clear in Fig. 7.3(a) and (b). The microstructures with high volume fraction of ferrite is more ductile instead of more martensite. On the other hand, the fitness indicates the alloy with the balance of strain and stress. The highest fitness alloy is the one improves the US and UTS simultaneously. Also, for Fe-C-Mn-Si alloy, the it is not necessary to suppress the martensite to achieve the highest fitness point.

In Fig. 7.3(c), the highest fitness alloy is the one with highest volume fraction of retained austenite. Considering bainite, the trend is not obvious but the optimum Vf(Bai) is about 50-60% to maximize fitness. In these calculations, the maximized ferrite or martensite improves elongation or strength respectively. According to the

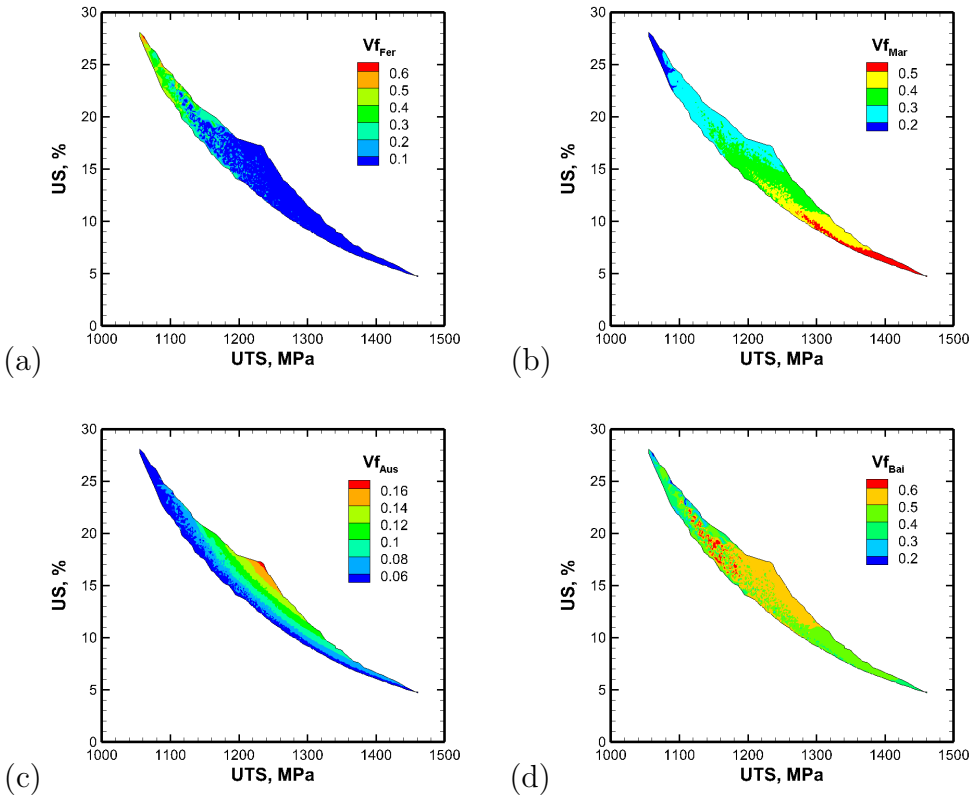

Figure 7.3: The relations of the mechanical properties and phase constituent

proposed model in this work, the optimum microstructure for conventional TRIP steel is the one with maximized volume fraction of austenite.

The selection of the chemical composition is the starting point of the designing procedure. The effects of carbon, manganese and silicon are summarized in Fig. 7.4. As Fig. 7.4(a), low carbon content alloy creates high volume fraction of ferrite. To maximize the fitness, high carbon content (0.5 wt%) is necessary. The effect of w_C^γ is different from the nominal carbon content. High w_C^γ is essentially increasing the stability of the retained austenite in high volume fraction of martensite microstructure which also possesses high strength. With the predicted Vf(Fer) and Vf(Mar) in Fig. 7.3, the high w_C^γ can be created by high T_{IA} and low T_{BIT} treatment.

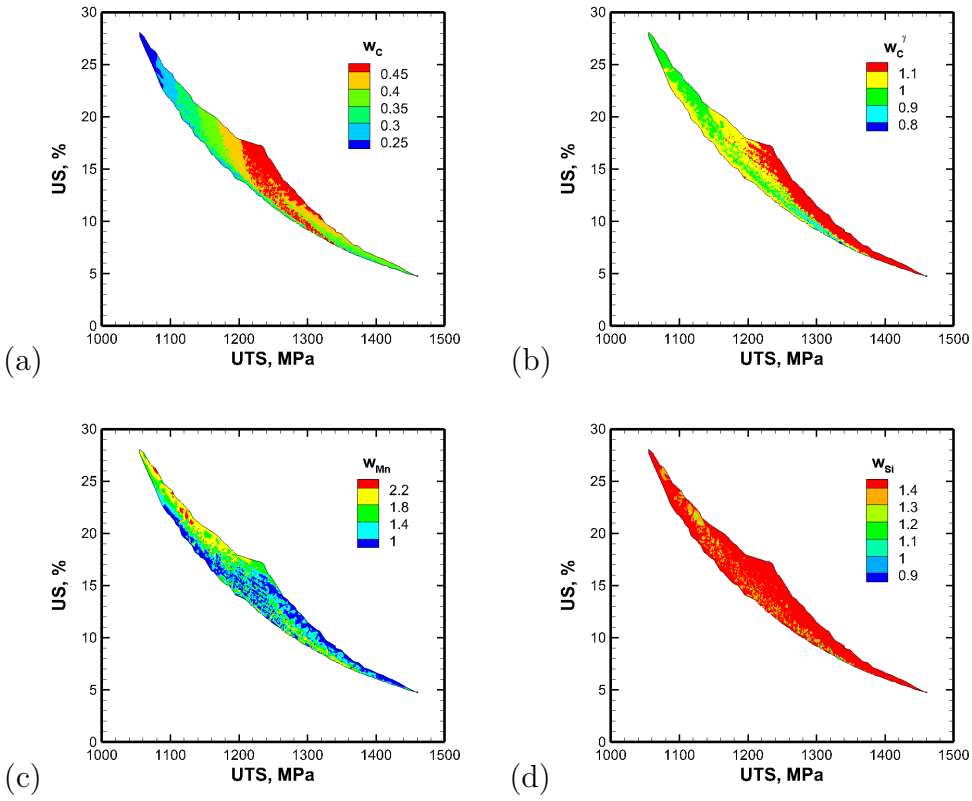

Figure 7.4: The chemical composition of the alloy with different mechanical properties

High manganese stabilizes retained austenite and increases the strain; but, maximizing Mn may not be necessary to achieve maximum fitness point. Different from Mn, the high silicon content is required to suppress the formation of cementite. Therefore, in general, the high Si is preferred for TRIP steel.

7.1.2 Kinetics Limitation

As mentioned in previous chapters, the kinetic model corresponds to the upper bound of the carbon enrichment in retained austenite. Due to the heavy loading of the time involved calculations, these series of optimization only includes 10 individulas and 500 generations. The targets are the same and therefore, the maximum

15,000 calculations can be expected. 2548 effective results are collected after the calculations.

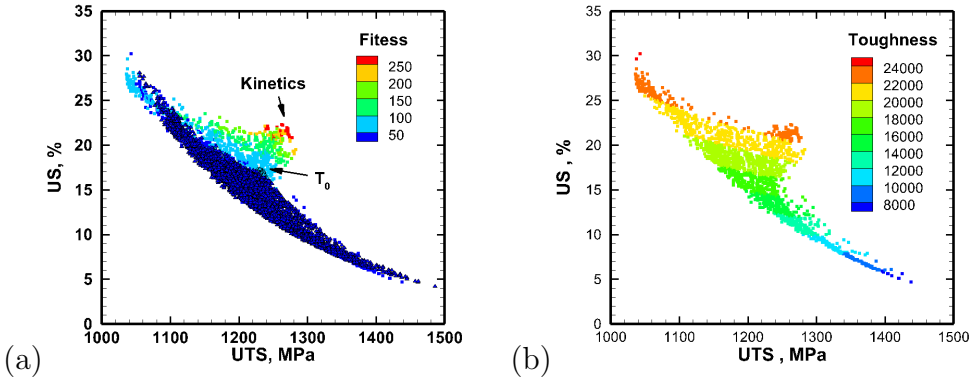

Figure 7.5: The predicted mechanical properties based on kinetic limitation (a) the calculated fitness comparing to the T_0 limitation (b) the predicted toughness (MPa%)

Fig. 7.5 is the predicted mechanical properties with fitness and toughness. Comparing to the calculations with T_0, the kinetic model allows more austenite to be retained after heat treatment and the highest fitness is also higher. More possible heat treatment can be applied in Fe-C-Mn-Si alloy; therefore, the highest toughness is higher than the predictions by T_0. As well as the US-UTS, both the properties can be improved by about 5 % and 40 MPa. The comparison can be shown in Table 7.3. This means that the non-homogeneous carbon distribution increases w_C^γ and this prevents the martensitic transformation in the end of the BIT treatment which increases the volume fraction of retained austenite. The mechanical properties have therefore been improved.

According to the T_0 and kinetic limitations, the optimum parameters including the chemical composition and heat treatments are listed in Table 7.2. It is shown

Table 7.2: The optimum parameters for maximizing fitness of Fe-C-Mn-Si alloy

Condition	w_C	w_{Mn}	w_{Si}	T_{IA}	T_{BIT}
T_0	0.50	1.44	1.50	>1096	638
Kinetics	0.50	1.98	1.50	>1045	675

that high carbon and silicon contents are preferred for improving the fitness in both cases. The selections of Mn concentration are not the same: 1.44 wt% for T_0 and 1.98 wt% for kinetic case. It can be understood by Fig. 2.1 that in T_0 case, increasing of Mn shifts both T_0 and T_{Ms} down. So, the adding of Mn does not affect the volume fraction of bainite and martensite too much. This is the reason why 1.44 wt% is the optimum Mn content in T_0 case. With the relation between T_{Ms} and kinetic limitation and the 4 wt% total amount of alloying, about 1.98 wt% Mn content is the optimum one.

The heat treatment for these two alloys are optimized while T_{IA} is higher than Ac_1 and T_{BIT} is at 638 and 675 Kelvin respectively. Along with these parameters, the predicted microstructure as well as the mechanical properties are listed as Table 7.3. In these two microstructures, the kinetic one is with higher Vf(Aus), w_C^γ and Vf(Bai). High Vf(Aus) and low Vf(Mar) improves the elongation significantly. The slightly increased w_C^γ improves the UTS also. With the calculations, for low alloying Fe-C-Mn-Si TRIP steel that the optimum chemical composition and the heat treatment are recommended as Table 7.2.

Table 7.3: The predicted microstructure and mechanical properties following Table 7.2

Condition	Vf(Aus)	Vf(Bai)	Vf(Fer)	Vf(Mar)	w_C^γ, wt%	US, %	UTS, MPa
T_0	0.17	0.57	0.00	0.26	1.16	17.0	1235
Kinetics	0.31	0.61	0.00	0.08	1.28	21.9	1270

7.2 Fe-C-Mn-Si-Al-Cr-Ni TRIP Steel

The conventional TRIP steel includes the chemical composition of C, Mn, and Si. A further step of optimization takes Al Cr and Ni into account as Table 7.1. It is reported that Al retards the formation of cementite and accelerates the bainitic transformation [26, 37]. Ni and Cr not only improve the mechanical properties but also stabilize austenite and lower T_{Ms} [84, 48]. It can be expected that Al can be used to replace Si as well as the role Ni and Cr play to Mn.

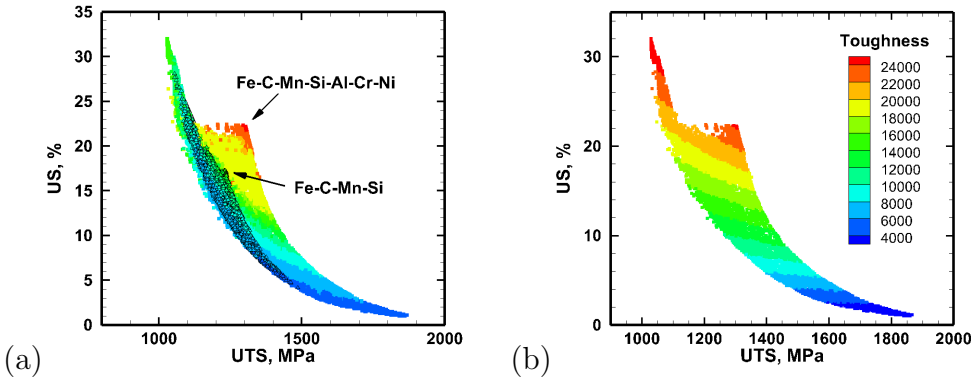

Figure 7.6: The predicted mechanical properties based on T_0 limitation (a) the calculated fitness comparing to the T_0 limitation (b) the predicted toughness (MPa%)

Following the same three optimizing conditions, each process includes 10 individual, 10,000 generations under T_0 limitation. The total 24,678 effective results are included in Fig. 7.6. Fig. 7.6(a) also includes the results in Fe-C-Mn-Si alloy as the black outline symbols. The adding of Al-Cr-Ni obviously extend the US-UTS domain under the same calculating criteria. It is the same as the conventional TRIP steel, the highest fitness locates in the middle of the extreme US or UTS cases. The optimum conditions for maximum fitness are listed in Table 7.4. As the previous cases,

the carbon content is recommended as the maximum, 0.5 wt%. Mn and Si contents are not as high as the Fe-C-Mn-Si alloy. As for the alternative elements, Cr and Ni are not preferred. A significant amount of Al, 0.76 wt% is suggested in this case. From the recommended chemical composition, it can be realized that the austenite stabilizer is not as important as the composition necessary to suppress cementite formation. It may because the carbon, the most important austenite stabilizer, is significantly added into this alloy. The importance of the Mn is not dominated.

Table 7.4: The optimum parameters for maximizing fitness of Fe-C-Mn-Si alloy

Condition	w_C	w_{Mn}	w_{Si}	w_{Al}	w_{Cr}	w_{Ni}	T_{IA}	T_{BIT}
T_0	0.50	1.20	1.42	0.76	0.04	0.00	1044	575

After the recommended heat treatment, the predicted Vf(Aus) is higher because the martensite is suppressed in this case. The w_C^γ is also higher which higher the strength comparing to the conventional TRIP steel. The phase diagram for BIT treatment in Table 7.2, 7.4, and 7.5 as Fig. 7.7 indicates that 0.76 wt% Al can significantly suppress the para-equilibrium austenite-cementite formation. Even the other thermodynamic states, T_{Ms} and T_0 are not affected too much, the mechanical performance can be improved by increasing Vf(Aus), Vf(Bai), and w_C^γ as well as decreasing Vf(Mar) at the same time.

Table 7.5: The predicted microstructure and mechanical properties following Table 7.4; the w_C^γ, US, and UTS are in units of wt%, %, and MPa

Condition	Vf(Aus)	Vf(Bai)	Vf(Fer)	Vf(Mar)	w_C^γ	US	UTS
T_0	0.36	0.32	0.32	0.00	1.36	22.2	1303

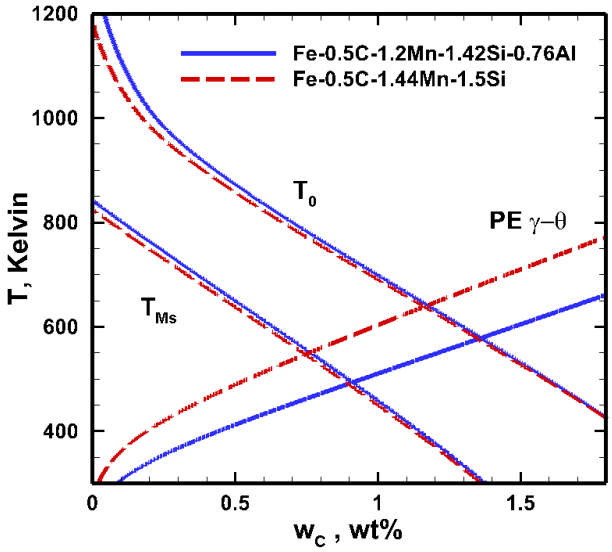

Figure 7.7: The predicted mechanical properties based on T_0 limitation (a) the calculated fitness comparing to the T_0 limitation (b) the predicted toughness (MPa%)

Fig. 7.8 contains similar analyses about the relations between chemical composition and mechanical performance. The diagrams for C Mn and Si are very similar to the previous ones: higher carbon ans silicon are preferred. The effects of the other three, Mn Cr and Ni, are not obvious. But the medium Al content (0.5-1.0 wt%) can significantly improve the mechanical performance by optimizing the microstructure.

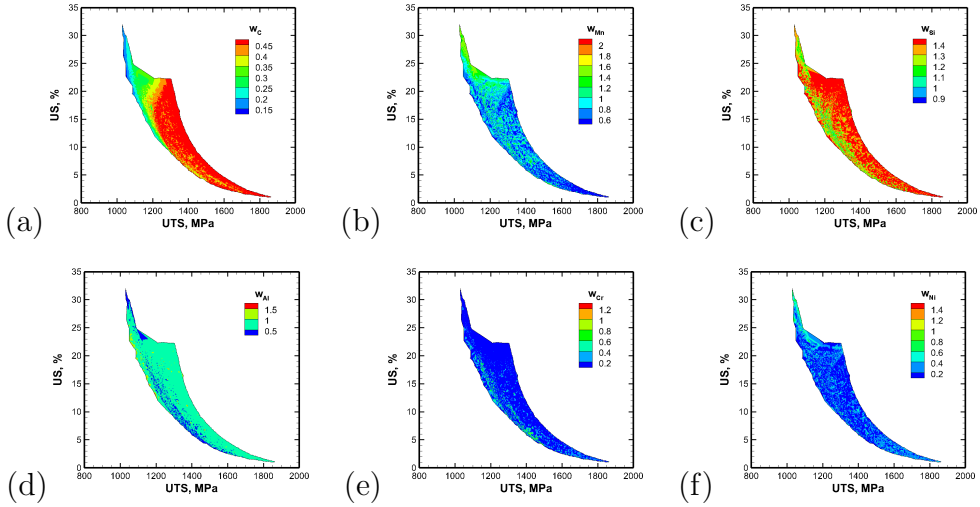

Figure 7.8: The predicted mechanical properties based on T_0 limitation (a) the calculated fitness comparing to the T_0 limitation (b) the predicted toughness (MPa%)

8. SUMMARY AND CONCLUSIONS

In this work, computational thermodynamics (CALPHAD) and kinetics are used to optimize the performance of TRIP-assisted steel. Including the chemical composition and temperatures for two-step treatment, there are up to 8 parameters are involved in designing process to optimize the microstructure for improving the mechanical performance.

In order to predict the alloy state after IA treatment, both para- and full equilibrium are considered. There is no powerful rule for selecting the heat treated temperature which depends on the chemical composition of the alloy. It is also found that the longer IA treated time allows the partitioning of the substitutional elements which stabilizes the austenite in general.

The thermodynamic limit for the bainitic transformation, T_0', is used to estimate the lower bound of the carbon saturation of retained austenite. Based on T_0', the kinetic model is developed for analysing the competition between carbon diffusion and phase transformation. The results explain that the non-homogeneous distribution of carbon further stabilizes the austenite against the martensitic transformation as it allows further enrichment of the austenite matrix.

Taking into consideration the $\gamma - \theta$ para-equilibrium condition for suppressing the formation of cementite, Fe-C-Mn-Si and Fe-C-Mn-Si-Al-Cr-Ni are designed using a genetic algorithm (GA) optimization process. GA is the numerical technique for efficiently searching the potential solutions in a defined domain using a properly defined fitness function. The selection and tests of the algorithm required parameters for this designing purpose are conducted in this work. For improving the mechanical properties, the fitness is proposed as $Vf(Aus)/(0.01w_C^{\gamma}(0.001 + Vf(Mar)))$. The

results recommend several recipes for these two kinds of alloys based on T_0 and kinetic limitations for BIT treatment. The designing guide is concluded as Fig. 8.1.

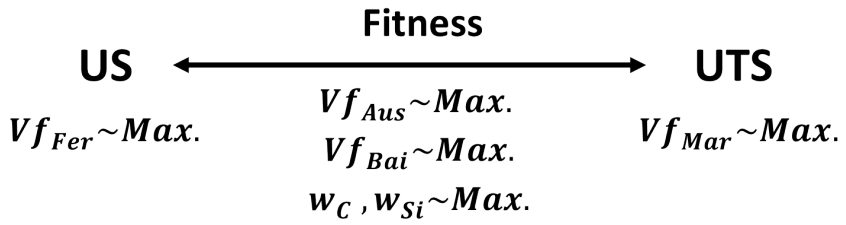

Figure 8.1: The guideline for designing TRIP steel

For high elongation requirements, the maximizing of the ferrite is recommended. On the other hand, for improving the strength, the martensite is significant. The optimum microstructure for TRIP steel is recommended as maximizing austenite and bainite simultaneously which can be achieved in high carbon and silicon content alloy with properly selected heat treatment. Because of the para-eq $\gamma - \theta$ condition and high carbon content, Mn is not as important as in the plain alloy; but a small amount of Al can improve the mechanical performance significantly. According to this model, Cr and Ni are not as important as the other elements even though their addition can stabilize the austenite.

In summary, this work represents one of the first instances in which a materials-by-design approach has been used to the optimization of the performance of a complex multi-phase microstructure. This approach, closely aligned to the Materials Genome initiative, is expected to be a powerful new tool that can accelerate the development of complex, multi-phase, multi-component structural materials.

REFERENCES

[1] M Abareshi and E Emadoddin. Effect of retained austenite characteristics on fatigue behavior and tensile properties of transformation induced plasticity steel. *Materials & Design*, 32(10):5099–5105, 2011.

[2] A. Ali and H. Bhadeshia. Nucleation of widmanstätten ferrite. *Materials Science and Technology*, 6(8):781–784, 1990.

[3] CM Amey, H Huang, and PEJ Rivera-Díaz-del Castillo. Distortion in 100cr6 and nanostructured bainite. *Materials & Design*, 35:66–71, 2012.

[4] J.O. Andersson and J. Agren. Models for numerical treatment of multicomponent diffusion in simple phases. *Journal of Applied Physics*, 72(4):1350–1355, 1992.

[5] KW Andrews. Empirical formulae for calculation of some transformation temperatures. *Iron and Steel Institute Journal*, 203(Part 7):721–727, 1965.

[6] H. Azizi-Alizamini, M. Militzer, and W.J. Poole. Austenite formation in plain low-carbon steels. *Metallurgical and Materials Transactions A*, pages 1–14, 2010.

[7] R.W. Balluffi, S.M. Allen, W.C. Carter, and R.A. Kemper. *Kinetics of Materials*. Wiley-Interscience, 2005.

[8] H. Bhadeshia. Driving force for martensitic transformation in steels. *Metal Science*, 15(4):175–177, 1981.

[9] H. Bhadeshia. Thermodynamic analysis of isothermal transformation diagrams. *Metal Science*, 16(3):159–166, 1982.

[10] H. Bhadeshia. Trip-assisted steels? *ISIJ International*, 42(9):1059–1060, 2002.

[11] H. Bhadeshia. Developments in martensitic and bainitic steels: role of the shape deformation. *Materials Science and Engineering: A*, 378(1):34–39, 2004.

[12] H.K.D.H. Bhadeshia. *Bainite in steels*. The Inst. of Materials, 2001.

[13] H.K.D.H. Bhadeshia. Phase transformations contributing to the properties of modern steels. *Bulletin of the Polish Academy of Sciences: Technical Sciences*, 58(2):255–265, 2010.

[14] FG Caballero, H. Bhadeshia, KJA Mawella, DG Jones, and P. Brown. Very strong low temperature bainite. *Materials Science and Technology*, 18(3):279–284, 2002.

[15] F.G. Caballero, M.K. Miller, AJ Clarke, and C. García-Mateo. Examination of carbon partitioning into austenite during tempering of bainite. *Scripta Materialia*, 63(4):442–445, 2010.

[16] F.G. Caballero, M.K. Miller, and C. García-Mateo. Carbon supersaturation of ferrite in a nanocrystalline bainitic steel. *Acta Materialia*, 58(7):2338–2343, 2010.

[17] F.G. Caballero, M.K. Miller, and C. García-Mateo. Slow bainite: an opportunity to determine the carbon content of the bainitic ferrite during growth. *Solid State Phenomena*, 172:111–116, 2011.

[18] F.G. Caballero, M.J. Santofimia, C. Garcia-Mateo, and C. Garcia de Andres. Time-temperature-transformation diagram within the bainitic temperature range in a medium carbon steel. *Materials Transactions*, 45(12):3272–3281, 2004.

[19] LC Chang. Bainite transformation temperatures in high-silicon steels. *Metallurgical and Materials Transactions A*, 30(4):909–916, 1999.

[20] LC Chang and H. Bhadeshia. Austenite films in bainitic microstructures. *Materials Science and Technology*, 11(9):874–882, 1995.

[21] S. Chatterjee and H. Bhadeshia. Transformation induced plasticity assisted steels: stress or strain affected martensitic transformation? *Materials Science and Technology*, 23(9):1101–1104, 2007.

[22] A.J. Clarke, J.G. Speer, D.K. Matlock, FC Rizzo, D.V. Edmonds, and M.J. Santofimia. Influence of carbon partitioning kinetics on final austenite fraction during quenching and partitioning. *Scripta Materialia*, 61(2):149–152, 2009.

[23] C. Coello Coello Coello and G. Toscano Pulido. A micro-genetic algorithm for multiobjective optimization. In *Evolutionary Multi-Criterion Optimization*, pages 126–140. Springer, 2001.

[24] T. Cool and H. Bhadeshia. Prediction of martensite start temperature of power plant steels. *Materials Science and Technology*, 12(1):40–44, 1996.

[25] T. De Cock, J.P. Ferrer, C. Capdevila, FG Caballero, V. Lopez, and C. García de Andrés. Austenite retention in low al/si multiphase steels. *Scripta Materialia*, 55(5):441–443, 2006.

[26] BC De Cooman. Structure-properties relationship in trip steels containing carbide-free bainite. *Current Opinion in Solid State and Materials Science*, 8(3-4):285–303, 2004.

[27] R.T. DeHoff. *Thermodynamics in Materials Science*. CRC Press, 2006.

[28] L. Delannay, P. Jacques, and T. Pardoen. Modelling of the plastic flow of trip-aided multiphase steel based on an incremental mean-field approach. *International Journal of Solids and Structures*, 45(6):1825–1843, 2008.

[29] D.W. Fan, H.S. Kim, and B.C. De Cooman. A review of the physical metallurgy related to the hot press forming of advanced high strength steel. *Steel Research International*, 80(3):241–248, 2009.

[30] S. Ganguly, S. Datta, and N. Chakraborti. Genetic algorithm-based search on the role of variables in the work hardening process of multiphase steels. *Computational Materials Science*, 45(1):158–166, 2009.

[31] A. García-Junceda, FG Caballero, C. Capdevila, C.G. de Andrés, et al. Effect of heating rate on reaustenitisation of low carbon niobium microalloyed steel. *Materials Science and Technology*, 24(3):266–272, 2008.

[32] C. García-Mateo and H. Bhadeshia. Nucleation theory for high-carbon bainite. *Materials Science and Engineering: A*, 378(1):289–292, 2004.

[33] D. Gaude-Fugarolas and P.J. Jacques. Modelling the kinetics of bainite transformation in steels. *Solid-Solid Phase Transformations in Inorganic Material*, 2:795–800, 2005.

[34] D. Gaude-Fugarolas and P.J. Jacques. A new physical model for the kinetics of the bainite transformation. *ISIJ International*, 46(5):712–717, 2006.

[35] G. Ghosh and GB Olson. Kinetics of fcc-bcc heterogeneous martensitic nucleation–i. the critical driving force for athermal nucleation. *Acta Metallurgica*, 42(10):3361–3370, 1994.

[36] D.E. Goldberg. *Genetic algorithms in search, optimization, and machine learning*. Addison-Wesley, 1989.

[37] M. Gomez, C.I. Garcia, D.M. Haezebrouck, and A.J. Deardo. Design of composition in (al/si)-alloyed trip steels. *ISIJ International*, 49(2):302–311, 2009.

[38] EB Hawbolt, B. Chau, and JK Brimacombe. Kinetics of austenite-pearlite transformation in eutectoid carbon steel. *Metallurgical and Materials Transactions A*, 14(9):1803–1815, 1983.

[39] RF HEHEMANN. Structure and growth of widmanstatten ferrite and bainite. In *Transformation and hardenability in steels: symposium*, page 15. Climax Molybdenum Company of Michigan, 1967.

[40] C. Hongbing et al. Thermodynamic prediction of ms and driving force for martensitic transformation in fe—mn—c alloys. *Acta Metallurgica*, 34(2):333–338, 1986.

[41] M. Huang, PEJ Rivera-Díaz-del Castillo, O. Bouaziz, and S. Van Der Zwaag. Modelling strength and ductility of ultrafine grained bcc and fcc alloys using irreversible thermodynamics. *Materials Science and Technology*, 25(7):833–839, 2009.

[42] K. Ishida. Calculation of the effect of alloying elements on the ms temperature in steels. *Journal of Alloys and Compounds*, 220(1-2):126–131, 1995.

[43] P Jacques, E Girault, T Catlin, N Geerlofs, T Kop, S van der Zwaag, and F Delannay. Bainite transformation of low carbon mnsi trip-assisted multiphase steels: influence of silicon content on cementite precipitation and austenite retention. *Materials Science and Engineering: A*, 273275(0):475 – 479, 1999.

[44] PJ Jacques. Transformation-induced plasticity for high strength formable steels. *Current Opinion in Solid State and Materials Science*, 8(3-4):259–265, 2004.

[45] PJ Jacques, Q. Furnemont, F. Lani, T. Pardoen, and F. Delannay. Multiscale mechanics of trip-assisted multiphase steels: I. characterization and mechanical testing. *Acta Materialia*, 55(11):3681–3693, 2007.

[46] A.I. Katsamas, G.N. Haidemenopoulos, and N. Aravas. Modelling of transformations in trip steels. *Steel Research International*, 75(11):737–743, 2004.

[47] A.I. Katsamas, A.N. Vasilakos, and G.N. Haidemenopoulos. Simulation of intercritical annealing in low-alloy trip steels. *Steel Res*, 71(9):351–356, 2000.

[48] S.J. Kim, C. Gil Lee, T.H. Lee, and C.S. Oh. Effect of cu, cr and ni on mechanical properties of 0.15 wt.% c trip-aided cold rolled steels. *Scripta Materialia*, 48(5):539–544, 2003.

[49] JS Kirkaldy. A zener–hillert model for growth of binary alloy cells. *Scripta Materialia*, 14(7):739–744, 1980.

[50] D.P. Koistinen and R.E. Marburger. A general equation prescribing the extent of the austenite-martensite transformation in pure iron-carbon alloys and plain carbon steels. *Acta Metallurgica*, 7(1):59 – 60, 1959.

[51] A. Konak, D.W. Coit, and A.E. Smith. Multi-objective optimization using genetic algorithms: A tutorial. *Reliability Engineering & System Safety*, 91(9):992–1007, 2006.

[52] E. Kozeschnik and H. Bhadeshia. Influence of silicon on cementite precipitation in steels. *Materials Science and Technology*, 24(3):343–347, 2008.

[53] M. Kuroda and S. Ikawa. Texture optimization of rolled aluminum alloy sheets using a genetic algorithm. *Materials Science and Engineering: A*, 385(1):235–244, 2004.

[54] A. Kutsov, Y. Taran, K. Uzlov, A. Krimmel, and M. Evsyukov. Formation of bainite in ductile iron. *Materials Science and Engineering: A*, 273:480–484, 1999.

[55] R. Kuziak, R. Kawalla, and S. Waengler. Advanced high strength steels for automotive industry. *Archives of Civil and Mechanical Engineering*, 8(2):103–117, 2008.

[56] F. Lani, Q. Furnémont, T. Van Rompaey, F. Delannay, PJ Jacques, and T. Pardoen. Multiscale mechanics of trip-assisted multiphase steels: Ii. micromechanical modelling. *Acta Materialia*, 55(11):3695–3705, 2007.

[57] HY Li, XW Lu, XC Wu, YA Min, and XJ Jin. Bainitic transformation during the two-step quenching and partitioning process in a medium carbon steel containing silicon. *Materials Science and Engineering: A*, 527(23):6255–6259, 2010.

[58] L. Li, BC De Cooman, P. Wollants, Y. He, and X. Zhou. Effect of aluminum and silicon on transformation induced plasticity of the trip steel. *Journal of Materials Science and Technology*, 20(2):135–138, 2004.

[59] L. Li, P. Wollants, ZY Xu, BC De Cooman, and XD Zhu. Effects of alloying elements on the concentration profile of equilibrium phases in transformation induced plasticity steel. *Journal of Materials Science & Technology*, 19(3):273–277, 2003.

[60] M.V. Li, D.V. Niebuhr, L.L. Meekisho, and D.G. Atteridge. A computational model for the prediction of steel hardenability. *Metallurgical and Materials Transactions B*, 29(3):661–672, 1998.

[61] S. Li, R. Zhu, I. Karaman, and R. Arryave. Thermodynamic analysis of two-stage heat treatment in {TRIP} steels. *Acta Materialia*, 60(17):6120 – 6130, 2012.

[62] S. Li, R. Zhu, I. Karaman, and R. Arryave. Development of a kinetic model for bainitic isothermal transformation in transformation-induced plasticity steels.

Acta Materialia, 61(8):2884 – 2894, 2013.

[63] H. Lukas, S.G. Fries, and B. Sundman. *Computational thermodynamics: the Calphad method*. Cambridge University press, 2007.

[64] Haiwen Luo, Jie Shi, Chang Wang, Wenquan Cao, Xinjun Sun, and Han Dong. Experimental and numerical analysis on formation of stable austenite during the intercritical annealing of 5mn steel. *Acta Materialia*, 59(10):4002 – 4014, 2011.

[65] NV Luzginova, L. Zhao, and J. Sietsma. Bainite formation kinetics in high carbon alloyed steel. *Materials Science and Engineering: A*, 481:766–769, 2008.

[66] J. Mahieu, BC De Cooman, and S. Claessens. Galvanizability of high-strength steels for automotive applications. *Metallurgical and Materials Transactions A*, 32(11):2905–2908, 2001.

[67] H. Matsuda and H.K.D.H. Bhadeshia. Kinetics of the bainite transformation. *Proceedings of the Royal Society of London. Series A: Mathematical, Physical and Engineering Sciences*, 460(2046):1707, 2004.

[68] O. Matsumura, Y. Sakuma, Y. Ishii, and J. Zhao. Effect of retained austenite on formability of high strength sheet steels. *ISIJ International*, 32(10):1110–1116, 1992.

[69] O. Matsumura, Y. Sakuma, and H. Takechi. Trip(transformation induced plasticity) and its kinetic aspects in austempered 0. 4 c–1. 5 si–0. 8 mn steel. *Scripta Materialia*, 21(10):1301–1306, 1987.

[70] O. Matsumura, Y. Sakuma, and H. Takechi. Retained austenite in 0. 4 c-si-1. 2 mn steel sheet intercritically heated and austempered. *ISIJ International*, 32(9):1014–1020, 1992.

[71] Javad Mola and Bruno C. De Cooman. Quenching and partitioning processing of transformable ferritic stainless steels. *Scripta Materialia*, 65(9):834 – 837, 2011.

[72] JM Oblak and RF Hehemann. Transformation and hardenability in steels. *Climax Molybdenum Co*, 15, 1967.

[73] C.S. Oh, H.N. Han, C.G. Lee, T.H. Lee, and S.J. Kim. Dilatometric analysis on phase transformations of intercritical annealing of fe- mn- si and fe- mn- si- cu low carbon trip steels. *Metals and Materials International*, 10(5):399–406, 2004.

[74] H.S. Park, O.H. Kwon, J.S. Baskin, B. Barwick, and A.H. Zewail. Direct observation of martensitic phase-transformation dynamics in iron by 4d single-pulse electron microscopy. *Nano Letters*, 9(11):3954–3962, 2009.

[75] D. Quidort and Y. Bréchet. The role of carbon on the kinetics of bainite transformation in steels. *Scripta Materialia*, 47(3):151–156, 2002.

[76] D. Quidort and YJM Brechet. Isothermal growth kinetics of bainite in 0.5% c steels. *Acta Materialia*, 49(20):4161–4170, 2001.

[77] D. Quidort and Y.J.M. Brechet. A model of isothermal and non isothermal transformation kinetics of bainite in 0.5% c steels. *ISIJ International*, 42(9):1010–1017, 2002.

[78] GI Rees and H. Bhadeshia. Bainite transformation kinetics part 1 modified model. *Materials Science and Technology*, 8(11):985–993, 1992.

[79] GI Rees and H. Bhadeshia. Bainite transformation kinetics part 2 non-uniform distribution of carbon. *Materials Science and Technology*, 8(11):994–1003, 1992.

[80] G. Renner and A. Ekárt. Genetic algorithms in computer aided design. *Computer-Aided Design*, 35(8):709–726, 2003.

[81] Y. Sakuma, O. Matsumura, and H. Takechi. Mechanical properties and retained austenite in intercritically heat-treated bainite-transformed steel and their variation with si and mn additions. *Metallurgical and Materials Transactions A*, 22(2):489–498, 1991.

[82] CP Scott and J. Drillet. A study of the carbon distribution in retained austenite. *Scripta Materialia*, 56(6):489–492, 2007.

[83] MM Souza, J.R.C. Guimarães, and KK Chawla. Intercritical austenitization of two fe-mn-c steels. *Metallurgical and Materials Transactions A*, 13(4):575–579, 1982.

[84] D.W. Suh, S.J. Park, H.N. Han, and S.J. Kim. Influence of al on microstructure and mechanical behavior of cr-containing transformation-induced plasticity steel. *Metallurgical and Materials Transactions A*, 41(13):3276–3281, 2010.

[85] K.C. Tan, T.H. Lee, and E.F. Khor. Evolutionary algorithms for multi-objective optimization: performance assessments and comparisons. *Artificial Intelligence Review*, 17(4):251–290, 2002.

[86] M. Umemoto, K. Tsuchiya, ZG Liu, and S. Sugimoto. Tensile stress-strain analysis of single-structure steels. *Metallurgical and Materials Transactions A*, 31(7):1785–1794, 2000.

[87] SMC Van Bohemen and J. Sietsma. Effect of composition on kinetics of athermal martensite formation in plain carbon steels. *Materials Science and Technology*, 25(8):1009–1012, 2009.

[88] J. Wang, S. van der Zwaag, Z. Yang, and H.S. Fang. Aspect ratio of bainite in steels. *Materials Letters*, 45(3-4):228–234, 2000.

[89] W. Xu, PEJ Rivera-Díaz-del Castillo, W. Wang, K. Yang, V. Bliznuk, LAI Kestens, and S. Van der Zwaag. Genetic design and characterization of novel ultra-high-strength stainless steels strengthened by ni3ti intermetallic nanoprecipitates. *Acta Materialia*, 58(10):3582–3593, 2010.

[90] M.A. Yescas and H. Bhadeshia. Model for the maximum fraction of retained austenite in austempered ductile cast iron. *Materials Science and Engineering: A*, 333(1):60–66, 2002.

[91] HL Yi, KY Lee, and H. Bhadeshia. Extraordinary ductility in al-bearing δ-trip steel. *Proceedings of the Royal Society A: Mathematical, Physical and Engineering Science*, 467(2125):234, 2011.

[92] H.L. Yi, K.Y. Lee, and H.K.D.H. Bhadeshia. Mechanical stabilisation of retained austenite in -trip steel. *Materials Science and Engineering: A*, 528(18):5900 – 5903, 2011.

[93] J.J. Yi, I.S. Kim, and H.S. Choi. Austenitization during intercritical annealing of an fe-c-si-mn dual-phase steel. *Metallurgical and Materials Transactions A*, 16(7):1237–1245, 1985.

[94] M. Zakeri, A. Bahrami, and SH Mousavi Anijdan. Using genetic algorithm in heat treatment optimization of 17-4ph stainless steel. *Materials & design*, 28(7):2034–2039, 2007.

[95] M. Zhang, L. Li, RY Fu, D. Krizan, and BC De Cooman. Continuous cooling transformation diagrams and properties of micro-alloyed trip steels. *Materials Science and Engineering: A*, 438:296–299, 2006.

[96] Z. Zhao, C. Liu, Y. Liu, and DO Northwood. A new empirical formula for the bainite upper temperature limit of steel. *Journal of Materials Science*,

36(20):5045–5056, 2001.

[97] R. Zhu, S. Li, I. Karaman, R. Arroyave, T. Niendorf, and H.J. Maier. Multi-phase microstructure design of a low-alloy trip-assisted steel through a combined computational and experimental methodology. *Acta Materialia*, 60(67):3022 – 3033, 2012.

APPENDIX A

CONFIGURATIONAL ENTROPY

In binary system, N_A and N_B are the number of A and B atoms in the system. The configurational entropy can be dpresented as [63, 27] :

$$S^{con} = kln(\frac{(N_A + N_B)!}{N_A!N_B!}) \tag{A.1}$$

According to Stirling's approximation, the equation can be simplified as:

$$\begin{aligned}
S^{con} &= kln(\frac{(N_A + N_B)!}{N_A!N_B!}) \\
&= k[(N_A + N_B)ln(N_A + N_B) - (N_A + N_B) - N_Aln(N_A) - N_A - N_Bln(N_B) - N_B] \\
&= k[(N_A + N_B)ln(N_A + N_B) - N_Aln(N_A) - N_Bln(N_B)] \\
&= k[N_Aln(N_A + N_B) + N_Bln(N_A + N_B) - N_Aln(N_A) - N_Bln(N_B)] \\
&= -k[N_Aln(\frac{N_A}{N_A + N_B}) + N_Bln(\frac{N_B}{N_A + N_B})] \\
&= -R[x_Aln(x_A) + x_Bln(x_B)]
\end{aligned}$$